

Sculpting of Martian brain terrain reveals the drying of ancient Mars

Shenyi Zhang^{a,b} , Lei Zhang^{a,*}, Yutian Ke^c, Jinhai Zhang^a

^a Institute of Geology and Geophysics, Chinese Academy of Sciences, Beijing, China

^b College of Earth and Planetary Sciences, University of Chinese Academy of Sciences, Beijing, China

^c Division of Geological and Planetary Sciences, California Institute of Technology, Pasadena, CA, USA

Corresponding authors: Lei Zhang

Email: zhangl@mail.igcas.ac.cn

Author Contributions: L.Z. conceived and designed the research; S.Z. analyzed data, developed codes, and conducted the numerical simulation; S.Z. and L.Z carried out the investigation. L.Z., Y.K., S.Z. and J.Z. interpreted the geological results. S.Z. and L.Z were responsible for visualization. L.Z. supervised the project. L.Z. and S.Z. wrote the original draft. All authors were involved in writing, reviewing and editing the final paper.

Competing Interest Statement: The authors declare that they have no competing interests.

Classification: Physical Sciences/Earth, Atmospheric, and Planetary Sciences

Keywords: Martian brain terrain; Self-organization; Sublimation; Mars paleoclimate; Freeze-thaw cycles.

Abstract

The Martian brain terrain (MBT), characterized by its unique brain-like morphology, is a potential geological archive for finding hints of paleoclimatic conditions during its formation period. The morphological similarity of MBT to self-organized patterned ground on Earth suggests a shared formation mechanism. However, the lack of quantitative descriptions and robust physical modeling of self-organized stone transport jointly limits the study of the thermal and aqueous conditions governing MBT's formation. Here we established a specialized quantitative system for extracting the morphological features of MBT, taking a typical region located in the northern Arabia Terra as an example, and then employed a numerical model to investigate its formation mechanisms. Our simulation results accurately replicate the observed morphology of MBT, matching its key geometric metrics with deviations $<10\%$. Crucially, however, we find that the self-organized transport can solely produce relief <0.5 m, insufficient to explain the formation of MBT with average relief of 3.29 ± 0.65 m. We attribute this discrepancy to sculpting driven by late-stage sublimation, constraining cumulative subsurface ice loss in this region to ~ 3 meters over the past ~ 3 Ma. These findings demonstrate that MBT's formation is a multi-stage process: initial patterning driven by freeze-thaw cycles (implying liquid water) followed by vertical sculpting via sublimation (requiring a dry environment). This evolution provides physical evidence for the transition of the ancient Martian climate from a wetter period to a colder hyper-arid state.

Significance Statement

The enigmatic Martian brain terrain (MBT) has long puzzled scientists. By combining quantitative modeling with geological analysis, we demonstrate that MBT is not the result of a single event but a multi-stage process. Its origin requires a stage of self-organized stone transport, followed by significant differential sublimation of subsurface ice that deepened the terrain. This specific sequence acts as a geological record, capturing a fundamental climatic transition on ancient Mars from a wetter, thawing environment to a cold, hyper-arid state. Our finding establishes a new paradigm for decoding the history of other icy landscapes, offering a clearer window into climate evolution of Mars and other planetary bodies.

Introduction

Martian brain terrain (MBT) is a potential archive of Martian paleo-climatic conditions found in the mid-latitudes of both the northern and southern hemispheres on Mars (1–5) (Figs. 1A). The close association with glacial landforms (3, 6–13) and the symmetrical distribution of MBT (2, 4, 14, 15) (SI Appendix, Fig. S1A) indicate that MBT's formation was controlled by ice/water activities and global climate conditions. These possible processes shaped the MBT's unique morphological pattern, which closely resembles the folds and ridges of human brain (Fig. 1C). Therefore, the distinct morphological feature of MBT is central to understanding its formation mechanism and ultimately provide key insights into the ice/water activities as well as the ancient climate conditions on Mars.

Over the past few decades, the formation mechanism of MBT has been debated. MBT was first identified in Mars Orbiter Camera (MOC) images (16) and was subsequently proposed to be the result of thermal processes (17). Levy et al., (2009) categorized MBT into open- and close-cell based on its morphology, and proposed a fracture-subsidence model to explain the development of MBT (1). A related study of terrestrial analogs compared the differences in morphology between the analogs and MBT, suggesting a potential role for aeolian processes in the formation of MBT (2).

Recently, the possibility garnered significant attention that MBT is analogous to the self-organized patterned ground on Earth periglacial regions, which is formed through the transport of stones driven by repeated freeze-thaw cycles (18–20, 5) (Fig. 1D). Orbital observations suggested that stones are widespread on Martian surface and clusters of stones are also present (12, 19, 21–24) (Fig. 1E), supporting the hypothesis. However, these hypotheses lack numerical validation because the quantitative morphological parameters and numerical simulation for MBT are lacking.

On the one hand, due to the sinuous morphology of MBT, conventional morphological description indicators fail to quantitatively characterize the morphological features of MBT effectively. On the other hand, the lack of *in-situ* data makes it difficult to replicate the environmental conditions for MBT formation in laboratory settings. Thus, we established a specialized quantification system for characterizing the morphological features of MBT and develop numerical models to investigate its formation mechanism, clarifying the relationship between the MBT's morphological features and the paleoclimatic conditions and ice/water activities during its formation period.

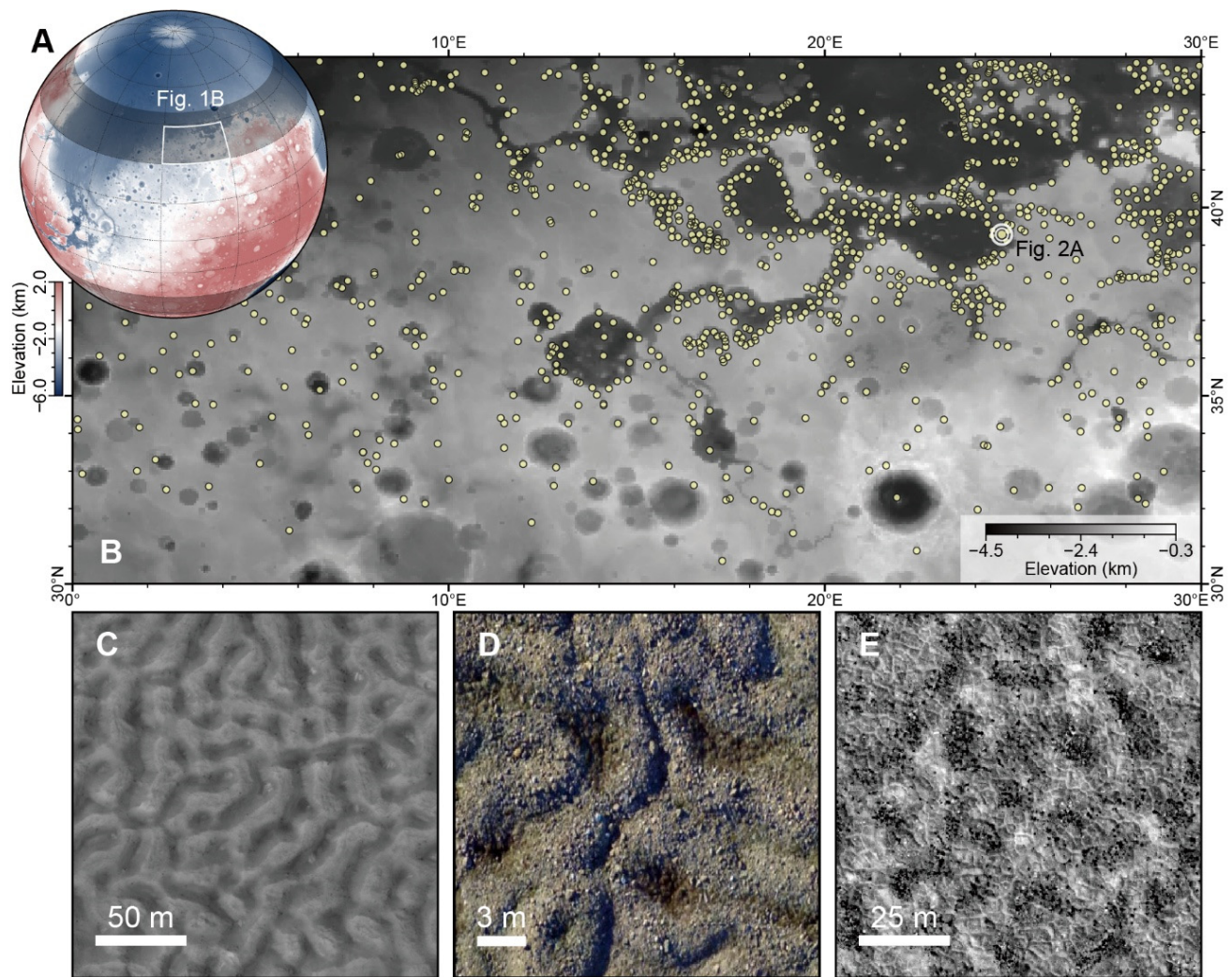


Figure 1. The distribution of brain terrain on Mars. **A.** Location map of the study area, with the base map of MOLA elevation data (64). The gray bands represent the latitude distribution range of MBT (4) (*SI Appendix*, Fig. S1A). **B.** Distribution of MBT in the study area with a scale bar on the bottom right. The yellow dots in the figure indicate the locations of Brain Terrain. **C.** Brain terrain in HiRISE image ESP_033165_2195 (NASA/JPL/University of Arizona). **D.** Pattern ground formed by self-organized stone transport in Dundas Harbor, Earth. (adapted from Hibbard et al., 2020 (65)) **E.** Densely distributed clusters of stones in HiRISE image ESP_026770_2525 (NASA/JPL/University of Arizona).

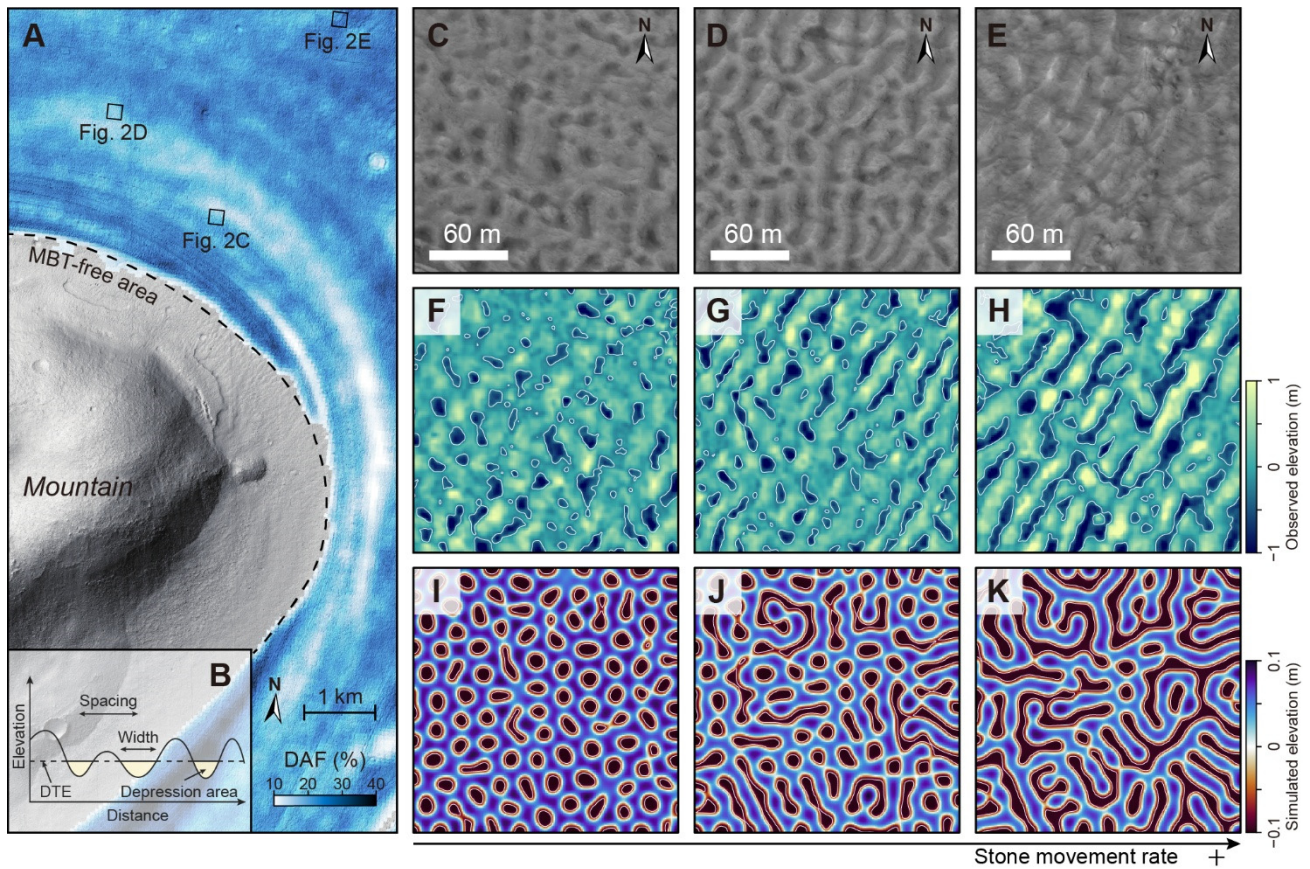


Fig. 2 Quantitative morphological metric extraction results and numerical simulation results. **A.** Spatial distribution of DAF across the study area, overlaid on a shaded relief base map derived from DTEEC_033165_2195_032875_2195_A01 (26). Colors represent specific DAF values indicated by the color bar on the bottom right. The MBT boundary is shown as a black dashed line. **B.** Schematic diagram defining the key morphological feature of MBT. The curve represents the terrain tangent of MBT. The yellow shaded areas indicate depression. The dashed line represents the depression threshold elevation (DTE) (see *SI Appendix*). **C-E.** HiRISE images of three local MBT in the study area. All three images share the same scale-bar. **F-H.** Detrended observed elevation data for three MBT areas shown in C-E, respectively (*SI Appendix*, Fig. S3). The white contour lines, which correspond to DTE values, outline the depression areas. Colors indicate elevation value using a color bar shown to the right of H. The **I-K.** Simulation results with increasing maximum stone movement rate (v_{max}): 3.25 mm/cycle (I), 3.40 mm/cycle (J) and 3.90 mm/cycle(K). Colors represent the simulated elevation using a common color bar shown to the right of K.

Results

Morphological parameter extraction

Following the mapping of MBT distribution in northern Arabia Terra on Mars (Fig. 1B), we selected a representative region (Fig. 1B and Fig. 2A) to derive quantitative morphological parameters of MBT. Based on the high-resolution digital terrain model (25), we conducted extraction of specific morphological parameters—depression area fraction (DAF), depression spacing (DS) and depression width (DW) (Fig. 2A; *SI Appendix*, Figs. S2 and S4). The extraction results of the study area show DAF ranging from $\sim 5\%$ to $\sim 40\%$, with average DS and DW of 27.18 ± 2.32 m and 7.90 ± 0.93 m, respectively. Further analysis shows that: The DS initially decreases and then increases with increasing DAF (Fig. 3A). In addition, DW shows a consistent increase with increasing DAF (Fig. 3B).

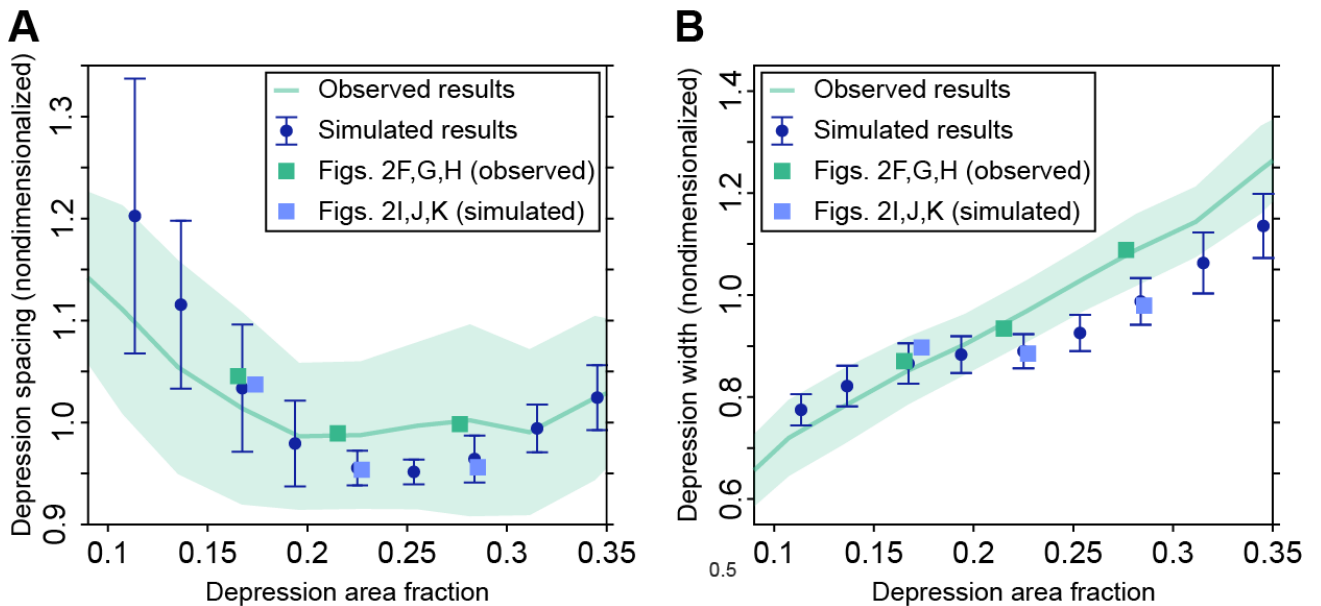


Fig. 3 Geometric Feature Extraction Results for MBT and Numerical Simulation. Panels A and B show the extraction results for DS and DW, respectively. The light green line represents the average of the geometric feature extraction results for the observed MBT, and the green shaded region denotes the standard deviation. The dark blue scatters with error bars (SD) represent the extraction results for numerical simulation (Error bars denote $\pm 2 \times \text{SD}$). The green and dark blue squares represent the extraction results of the MBT shown in the Fig. 2F-H and the simulated results shown in the Fig. 2I-K. The nondimensionalized depression spacing and width are defined as the ratio of depression spacing (width) to the average depression spacing (width) (*SI Appendix*, Fig. S6).

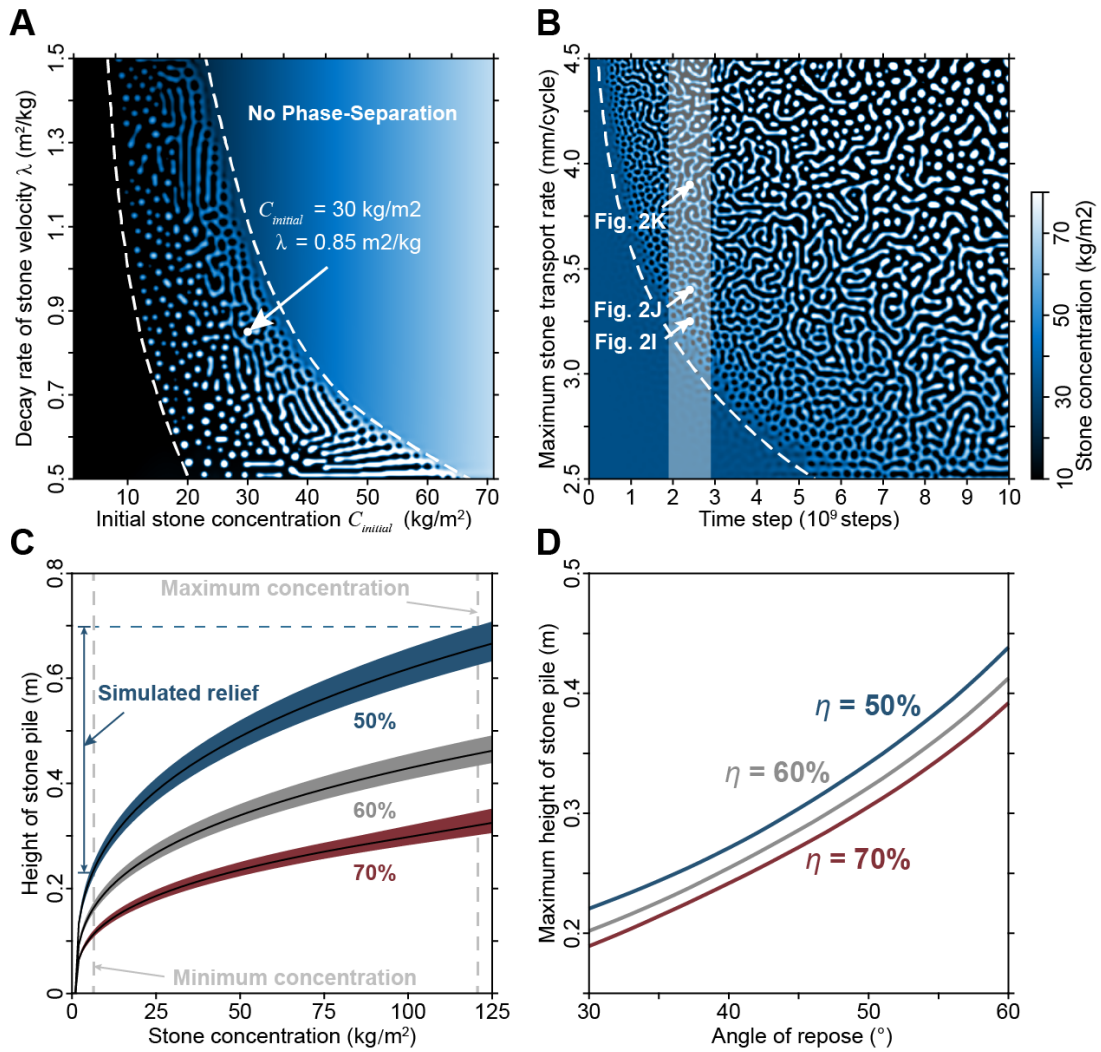


Fig. 4 Parameter scan results and simulated relief analysis. **A. Parameter scan results for λ and $C_{initial}$.** The dashed line indicates the boundary demarcating whether phase separation occurs or not. The white dot represents the parameter used in this study. This simulation was obtained under the parameter combination of $v_{max}=3.0 \text{ mm/cycle}$, $M = 1 \times 10^{-6}$, $d=2$, $\alpha=1$, $\kappa=0.225$, $t = 1 \times 10^{10} \text{ steps}$. **B. Parameter scan results for v_{max} and t .** The dashed line represents the temporal threshold at which phase separation begins to occur under different v_{max} . The three dots represent the parameter used in Figs. 2I-K. ($t = 2.4 \times 10^9 \text{ steps}$, $v_{max} = 3.25, 3.40, 3.90 \text{ mm/cycle}$, respectively). The shaded area represents the parameter range used in C. ($t = 1.9-2.9 \times 10^9 \text{ steps}$) **C. The theoretical curve of height of stone pile versus stone concentration.** The cyan, gray, and red shaded areas represent the results calculated for angles of repose (θ) ranging from 30° to 60° at packing density (η) of 50%, 60%, and 70%, respectively (see *SI Appendix*). The solid black line denotes the results for $\theta = 45^\circ$. The dashed lines represent the maximum/minimum stone concentration. The vertical distance between the intersection points of the solid line and the dashed line represents the simulated relief. (The relief is 0.2860 with $\theta=45^\circ$, $\eta=60\%$.) **D. The theoretical curve of maximum height versus angle of repose.** The three curves correspond to the spatial utilization rates of 50%, 60%, and 70% in panel C, respectively. The figure illustrates the simulated maximum relief under different model parameters.

The numerical simulation of self-organized stone transport

Self-organization is a common phenomenon in nature, with phase separation serving as a key physical principle for its description (26–29). It has been employed in simulation studies of landforms on Earth analogue to MBT (18, 20), proving that the distribution of stones exhibits characteristics of self-organization under freeze-thaw cycles. Here, based on the framework of self-organization, we develop a dynamic model to describe the spatial variations in stone concentration during the self-organized transport process. (see *SI Appendix*). We performed a parametric scan of λ , $c_{initial}$, v_{max} and t (see *SI Appendix*), identified the parameter range over which “brain-pattern” occurs (Figs. 4A and B), and successfully reproduced patterns highly similar to observed MBT (Figs. 2F-K; *SI Appendix*, Fig. S13). To quantitatively evaluate the accuracy of simulated results, we established a quantitative relationship between concentration and elevation (Figs. 4C; *SI Appendix*, Figs. S14 and S15) to map the simulated stone concentrations to elevation, enabling the extraction of quantitative morphological parameters. The results show close agreement: the deviation in the extracted morphological features between the simulation and the observed MBT results is less than 10%, with the DAF values obtained from the simulation results (17.39%, 22.73%, 28.55%; Figs. 2I-K) agreeing well with those from the observed MBT (16.53%, 21.52%, 27.65%; Figs. 2F-H), respectively. This close agreement extends to the DS and DW parameters. (Fig. 3). Besides these specific cases, simulated results obtained with v_{max} values ranging from about 2.9 to 4.15 mm/cycle remain consistent with the observed MBT results (Figs. 3; *SI Appendix*, Fig. S13G and H). However, it should be noted that the relief of the simulated results are significantly less than that of MBT in study area.

We tested the relationship between concentration and elevation under varying angles of repose (θ) and packing density (η) to discuss the maximum achievable relief in the simulation results (Figs. 4C and D; *SI Appendix*, Fig. S15). The calculation results show that the maximum relief does not exceed 0.5 m across all tested conditions (Fig. 4D). However, the observation of MBT in the study area reveals an average relief of 3.29 ± 0.65 m (*SI Appendix*, Fig. S16), which is obviously larger than 0.5 m. This discrepancy suggests that the formation of the MBT is complex and cannot be attributed solely to the self-organized transport of stones.

Discussion

The implication for the discrepancy between simulated and observed results

The discrepancy in relief between simulated and observed MBT (with <0.5 m and 3.29 ± 0.65 m, respectively) indicates a meter-scale modification process following the self-organization stage. Given that the modification process is characterized by meter-scale features, we rule out internal dynamic

geological processes (e.g., tectonism and volcanism) because they typically reshape terrain on a kilometer scale and leave distinct geological signatures like faults systems and volcano constructs. In contrast, the external dynamic geological processes typically modify planetary surface at far smaller scale. There are varieties of active external processes on present Martian surface, such as impact cratering, aeolian erosion, and sublimation of ice (30, 31). Impact cratering is ruled out because it is a local process and characterized by a random spatial distribution, which contrasts with the widespread and dense distribution of MBT. Aeolian erosion is unlikely to be the primary mechanism for the observed relief amplification as well. This process generally smooths topography by eroding highs and infilling lows, and thus cannot explain the development of the deep, regularly patterned depressions observed in MBT. Sublimation, a widespread process observed on the Martian surface (6, 16, 17), can modify terrain across a range of scales. It has been proven to play a key role in shaping glacial landscapes across the Martian mid-latitudes (see *SI Appendix*, Fig. S1A) (17, 31–34), thereby providing a robust explanation for the late-stage modification of the MBT. First, the occurrence of freeze-thaw cycles during the self-organization stage requires the presence of subsurface ice, which could subsequently supply material for the late-stage sublimation. Second, the sublimation process requires specific thermal conditions that allow ice to directly change from the solid to the gas phase. These conditions differ from those of freeze-thaw cycle, indicating that the two processes are unlikely to occur concurrently. This aligns with our hypothesis of a distinct, late-stage modification. Finally, the dense and contiguous distribution of the MBT (*SI Appendix*, Fig. S2) requires a modification process that is both widespread and capable of acting relatively uniformly across the region. As a common process widely observed on the Martian surface (6, 16, 17), sublimation could occur in nearly all ice-related landscapes under specific conditions fulfilling the distribution requirements of the MBT. Thus, sublimation is identified as the most likely process resulting in the late-stage modification of the MBT.

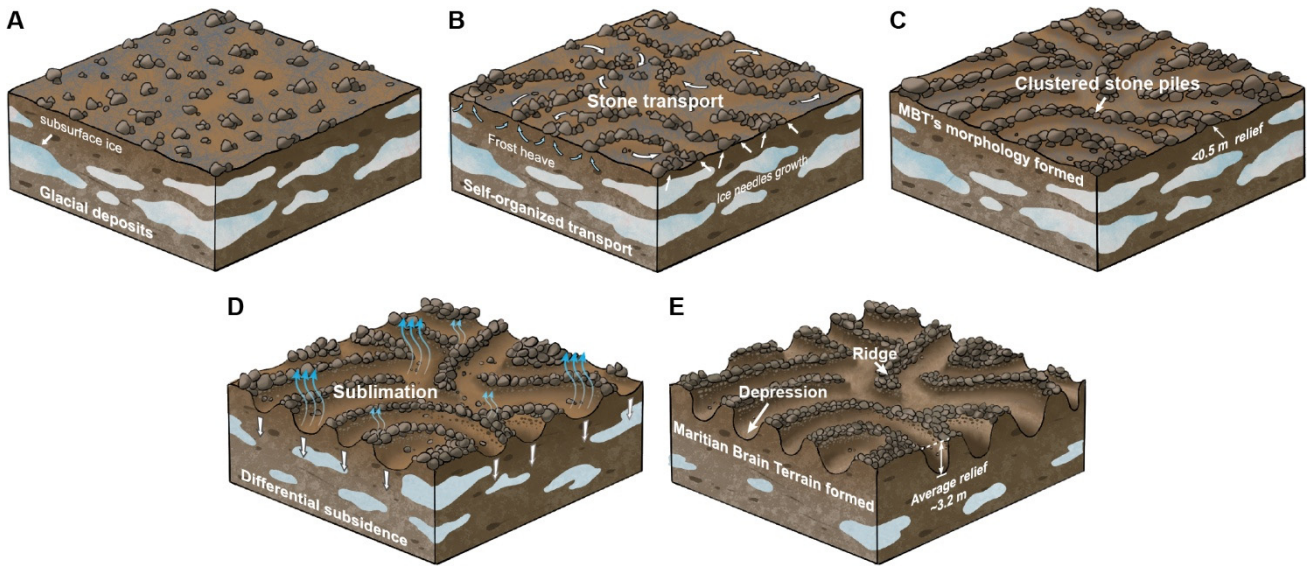


Fig. 5 The two-stage formation mechanism of Martian brain terrain. **A.** The early stage of MBT, stones are evenly distributed on the Martian surface. **B.** Driven by freeze-thaw cycles, stones undergo self-organized transport, forming brain-like patterns. The white arrows on the top surface indicate the stone transport. The blue arrows on the left-side represent the frost heaving process while white arrows on the right-side indicate the ice needles growth. **C.** The brain-like framework (clustered stone piles) formed after stone self-organized transport process. The raised stone piles represent the high stone concentration area, and the depression area represent the low stone concentration area. **D.** The differential sublimation effect enhanced the relief. The light blue arrows on the top surface represent the sublimation process and the white arrows on the left and right side indicate the subsidence driven by the sublimation process. **E.** The Martian brain terrain formed.

The implication for the multi-stage formation mechanism of MBT

Based on the simulation results and discussion, we propose a multi-stage formation mechanism for the MBT that involves an initial self-organization stage followed by a stage dominated by ice sublimation (Fig. 5). During the self-organization stage, glacial deposits rich in moisture and stones act as the basic material for MBT development (7, 35–38) with the stones distributed randomly on the deposit surface initially (Fig. 5A). Then, moisture migration, frost heave, and ice needle growth occur repeatedly within the sediments driven by freeze-thaw cycles (39–43), resulting in the transport of surface stones (20, 44–54) (Fig. 5B). In this stage, the stone displacements are concentration-based (20): The stones in high-concentration areas undergo smaller displacements than those in low-concentration areas, due

to the higher collision frequency of stones and the decline of needle ice growth. This results in a positive feedback mechanism: due to this differential displacement, stones transport from low-concentration areas to high-concentration areas, which further decreases the concentration in low-concentration area and increases it in high-concentration areas. However, stone concentration cannot increase infinitely. Due to spatial and gravitational constraints, the stone clusters will collapse in high-concentration areas, which leads to a decrease in concentration. This establishes a negative feedback mechanism at the macroscopic scale. Both the negative and positive feedback mechanisms trigger the self-organized patterns, causing the spatial distribution of stones to gradually shift from a random and disordered arrangement to a regular and orderly one (Fig. 5C). Ultimately, MBT morphology is formed by the self-organized transport of stones under repeated freeze-thaw cycles.

After the self-organization stage, the stone clusters formed, analogous to those shown in Fig. 1D, resulting in an initial relief (Fig. 5C). In areas of low stone concentration, the nearly exposed ice-rich deposits sublimate efficiently (33, 55–61), leading to a higher sublimation rate than that in high-concentration areas and resulting in significant differential sublimation. Additionally, the albedo feedback caused by the surface depression enables the depression floors to receive more solar radiation than the surrounding surfaces (62). This process further enhances differential sublimation, thereby accelerating the growth of vertical relief. Ultimately, through the processes of self-organized transport of stone and subsequent differential sublimation, the MBT formed (Fig. 5E).

The multi-stage formation mechanism indicates that the formation of MBT involves two distinct stages, reflecting a transition from a climate period dominated by freeze-thaw cycles to one governed by sublimation. The freeze-thaw cycle requires conditions that periodically sustain liquid water, implying a warmer and wetter paleoclimate. In contrast, sublimation requires colder, drier conditions that permit the direct transition of ice from the solid to the gas phase. Thus, the MBT serves as a geological archive recording a paleoclimatic transition from periodic warm and wet conditions to persistent cold and dry ones.

The crater dating statistics of fresh impact craters on the MBT within the Ismenius Lacus (including our study area) (5) indicate a surface stabilization age of 2.9 ± 0.3 Ma, suggesting that the first-stage evolution of the MBT in this area ceased at this time. In addition, the distribution of fresh and

moderately degraded craters indicates that MBT evolution commenced at 23.1 ± 1.4 Ma (5). These ages correspond to the period of high-to-low obliquity transition (~ 5 -3 Ma) and a high obliquity period (~ 20 Ma) (63), respectively, strongly suggesting that MBT formation is closely linked to variations in Martian obliquity. Collectively, this evidence demonstrates that the MBT is a geological archive of paleoclimatic change, consistent with our proposed multi-stage model.

Estimation of the sublimation modification rate on Mars

To constrain the magnitude of late-stage sublimation modification, we focus on the topographic difference between the observed MBT and our self-organization simulations. Our results indicate that sublimation must have increased the topographic relief by approximately 3.0 meters ($\theta=45^\circ$, $\eta=60\%$) after the initial self-organization stage. This value represents the minimum cumulative sublimation-driven modification that has occurred since the terrain stabilized around $\sim 2.9 \pm 0.3$ Ma (5). Such a multi-meter scale of modification is consistent with the slow, long-term sublimation rates inferred for shallow subsurface ice on Mars (33, 55–61). Therefore, the estimate of ~ 3 meters of cumulative sublimation provides a critical constraint that must be satisfied by future quantitative models of sublimation rates specific to MBT landscapes.

Based on a quantitative analysis of MBT morphology, we conducted simulation to investigate its formation mechanism. The self-organization model alone cannot explain the discrepancy in relief. Therefore, we propose a multi-stage model to explain the formation of MBT which implies a paleoclimatic transition from warm to cold conditions. It should be noted that our results constrain the cumulative sublimation modification rather than the specific parameters governing the process, such as its rate, critical conditions or substrate dependence. Future *in-situ* samples from Mars will provide critical constraints and deepen the understanding of MBT formation.

Conclusion

In this study, we established quantitative morphological parameters (DAF, DS and DW) to characterize the MBT and successfully reproduced its brain-like pattern using a dynamic model of self-organized transport of stone. Our results reveal a multi-stage formation mechanism—initial patterning followed

by late-stage sculpting via sublimation. We interpret this evolution as a record of Martian paleoclimate transition from warm to cold conditions. The quantified magnitude of late-stage sublimation provides a critical constraint for this landscape. Collectively, these findings demonstrate that Martian brain terrain (MBT) serves as a key archive for understanding paleoclimatic conditions and ice/water activities in the mid-latitudes, providing critical context for future missions targeting water ice detection, habitability studies and paleoclimate reconstruction on Mars.

Materials and Methods

The quantified morphological parameters of MBT. We introduce three parameters to quantitatively characterize Martian Brain Terrain (MBT): Depression Area Fraction (DAF), Depression Spacing (DS), and Depression Width (DW). These metrics are defined as follows: **1)** Depression Area Fraction (DAF): The proportion of the study area in which the elevation is below the Depression Threshold Elevation (DTE; *see SI Appendix*); **2)** Depression Spacing (DS): The average distance between depression centers within the study area; **3)** Depression Width (DW): The average width of depressions within the study area. These metrics are designed to capture the average morphological properties of an MBT region, not the detailed geometry of individual depressions. Their values are scale-dependent. Therefore, to ensure consistency, all analyses in this study are based on a uniform spatial evaluation unit of 200 m × 200 m (*see SI Appendix*). All subsequent discussions and comparisons involving DAF, DS and DW refer to measurements derived from this fixed scale.

Extraction of MBT morphological parameters. We developed a novel method, termed “Rotation-Slicing Method” (*see SI Appendix*), to extract quantitative morphological parameters from MBT. This method characterizes regional morphology through systematic multi-angle topographic profiling and consists of three steps: **1)** Profile Acquisition: A set of equal-length topographic profiles at various angles was systematically sampled across the study area according to a predefined pattern (*SI Appendix, Fig.S4A*). **2)** Profile Analysis: Each profile was analyzed to identify depressions. For profiles intersecting depressions, the distance between successive depression bases and the width of each depression were calculated (*SI Appendix, Fig.S4B*). **3)** Data Aggregation: The spacing and width

measurements from all profiles were arithmetically averaged. The regional Depression Spacing (DS) value is defined as this average spacing and the Depression Width (DW) value as the average width.

Phase-separation based self-organization model. Building upon the Cahn-Hilliard theory of phase separation, we develop a dynamic model to describe the self-organized transport of stones and the formation of brain-like patterns under freeze-thaw cycles. The model is founded on the core assumption that the local transport velocity of stones is negatively correlated with their local concentration—movement is slower in high-concentration areas and faster in low-concentration areas. This feedback mechanism drives the phase-separation behavior. The model takes the stone concentration, c , as the variable, and its evolution follows the mass conservation equation:

$$\frac{\partial c}{\partial t} = -M\nabla J \quad (\text{Eq. 1})$$

where M is the coefficient governing the diffusion rate, and the flux J is given by:

$$J = -D\nabla c - \frac{c}{2}D' + \kappa\nabla(\nabla^2 c) \quad (\text{Eq. 2})$$

$$D = \gamma v(c)^2 \quad (\text{Eq. 3})$$

Here, D denotes the concentration-dependent diffusion coefficient, γ represents the strength of the spatial collision frequency, and v is the stone transport velocity. The first two terms in Eq. (2) together describe a mechanistic diffusive flux. The third term is a higher-order gradient term with coefficient $\kappa > 0$, which controls the interfacial width of the evolving pattern. By combining Eq. (2) and (3) with Eq. (1), the governing equation of the model is obtained. (see *SI Appendix*)

$$\frac{\partial c}{\partial t} = M\nabla^2(G(c) - \kappa\nabla^2 c) \quad (\text{Eq. 4})$$

Topographic reconstruction based on an idealized stone pile model. To simulate the three-dimensional morphology of self-organized landforms, we establish a mapping from the two-dimensional stone concentration distribution to topographic height. This mapping relies on an idealized model in which all stones within a unit area are assumed to form a conical pile (see *SI Appendix*, Fig. S14). For a given stone mass per unit area (i.e., stone concentration), the height of this pile depends solely on its angle of repose (θ), the packing density (η), and the stone density (ρ_{stone}). (see *SI*

Appendix) This idealized model yields the following relationship between stone concentration (c) and pile height (H_{pile}):

$$c = \frac{\pi}{3} \cdot H_{pile}^3 \cdot \tan\theta^{-2} \cdot \eta \cdot \rho_{stone} \quad (\text{Eq. 5})$$

By testing different angles of repose and packing densities, we generated three-dimensional topographic data for brain-shaped landforms under various stone accumulation models. In this study, we used an angle of repose (θ) of 45° , a packing density (η) of 60%, and a stone density (ρ_{stone}) of 2000 kg m^{-3} , representing a state of strong interlocking and moderate packing.

Acknowledgments

This work is supported by the National Natural Science Foundation of China (Grants No. 42441810 and 42204178). This work utilized MATLAB for morphological parameters extraction, and COMSOL Multiphysics (version 6.2, <https://www.comsol.com/>) for model computation, specifically employing its Phase Field module (<https://www.comsol.com/model/phase-separation-2054>). The Arc Geographic Information System (ArcGIS, version 10.8, <https://www.esri.com/en-us/arcgis/geospatial-platform/overview>) was employed for geospatial data processing, High Resolution Imaging Science Experiment (HiRISE) imagery and Digital Terrain Models (DTM) data for topographic context (<https://www.uahirise.org/>). The MATLAB code for geometric feature extraction and result visualization is available at <https://github.com/zhanglei911/BrainTerrainOnMars>. Data associated with this research are available and can be obtained by contacting the corresponding author.

References

1. J. S. Levy, J. W. Head, D. R. Marchant, Concentric crater fill in Utopia Planitia: History and interaction between glacial “brain terrain” and periglacial mantle processes. *Icarus* **202**, 462–476 (2009).
2. R.-L. Cheng, H. He, J. R. Michalski, Y.-L. Li, L. Li, Brain-terrain-like features in the Qaidam Basin: Implications for various morphological features on Mars. *Icarus* **363**, 114434 (2021).
3. A. Bina, G. R. Osinski, Decameter-scale rimmed depressions in Utopia Planitia: Insight into the glacial and periglacial history of Mars. *Planetary and Space Science* **204**, 105253 (2021).
4. K. A. Pearson, E. Noe, D. Zhao, A. Altinok, A. M. Morgan, Mapping “Brain Terrain” Regions on Mars Using Deep Learning. *Planet. Sci. J.* **5**, 167 (2024).

5. A. M. Morgan, E. Z. Noe Dobrea, K. A. Pearson, A. Altinok, Crater Retention Timescales of Brain Coral Terrain Record Past Climatic Change on Mars. *Planet. Sci. J.* **6**, 200 (2025).
6. J. Levy, J. Head, D. Marchant, Thermal contraction crack polygons on Mars: Classification, distribution, and climate implications from HiRISE observations. *J. Geophys. Res.* **114**, 2008JE003273 (2009).
7. J. Levy, J. W. Head, D. R. Marchant, Concentric crater fill in the northern mid-latitudes of Mars: Formation processes and relationships to similar landforms of glacial origin. *Icarus* **209**, 390–404 (2010).
8. J. S. Levy, J. W. Head, D. R. Marchant, Gullies, polygons and mantles in Martian permafrost environments: cold desert landforms and sedimentary processes during recent Martian geological history. *Geological Society, London, Special Publications* **354**, 167–182 (2011).
9. C. Souness, B. Hubbard, R. E. Milliken, D. Quincey, An inventory and population-scale analysis of martian glacier-like forms. *Icarus* **217**, 243–255 (2012).
10. R. K. Sinha, S. Vijayan, Geomorphic investigation of craters in Alba Mons, Mars: Implications for Late Amazonian glacial activity in the region. *Planetary and Space Science* **144**, 32–48 (2017).
11. C. Gallagher, F. E. G. Butcher, M. Balme, I. Smith, N. Arnold, Landforms indicative of regional warm based glaciation, Phlegra Montes, Mars. *Icarus* **355**, 114173 (2021).
12. G. Driver, M. R. El-Maarry, B. Hubbard, S. Brough, Large Glacier-Like Forms on Mars: Insights From Crater Morphologies and Crater Retention Ages. *JGR Planets* **129**, e2023JE008207 (2024).
13. X. Xu, *et al.*, Shallow Water Ice Detection From SHARAD Data in Central Utopia Planitia, Mars. *JGR Planets* **130**, e2023JE008145 (2025).
14. E. Hauber, S. Van Gasselt, M. G. Chapman, G. Neukum, Geomorphic evidence for former lobate debris aprons at low latitudes on Mars: Indicators of the Martian paleoclimate. *J. Geophys. Res.* **113**, 2007JE002897 (2008).
15. J. S. Levy, C. I. Fassett, J. W. Head, C. Schwartz, J. L. Watters, Sequestered glacial ice contribution to the global Martian water budget: Geometric constraints on the volume of remnant, midlatitude debris-covered glaciers. *J. Geophys. Res. Planets* **119**, 2188–2196 (2014).
16. M. C. Malin, K. S. Edgett, Mars Global Surveyor Mars Orbiter Camera: Interplanetary cruise through primary mission. *J. Geophys. Res.* **106**, 23429–23570 (2001).
17. N. Mangold, Geomorphic analysis of lobate debris aprons on Mars at Mars Orbiter Camera scale: Evidence for ice sublimation initiated by fractures. *J. Geophys. Res.* **108**, 2002JE001885 (2003).
18. M. A. Kessler, B. T. Werner, Self-Organization of Sorted Patterned Ground. *Science* **299**, 380–383 (2003).
19. C. Gallagher, M. R. Balme, S. J. Conway, P. M. Grindrod, Sorted clastic stripes, lobes and associated gullies

in high-latitude craters on Mars: Landforms indicative of very recent, polycyclic ground-ice thaw and liquid flows. *Icarus* **211**, 458–471 (2011).

20. A. Li, *et al.*, Ice needles weave patterns of stones in freezing landscapes. *Proc. Natl. Acad. Sci. U.S.A.* **118**, e2110670118 (2021).
21. E. Hébrard, *et al.*, An aerodynamic roughness length map derived from extended Martian rock abundance data. *J. Geophys. Res.* **117**, 2011JE003942 (2012).
22. G. A. Morgan, *et al.*, Availability of subsurface water-ice resources in the northern mid-latitudes of Mars. *Nat Astron* **5**, 230–236 (2021).
23. A. L. Cohen-Zada, D. R. Hood, R. C. Ewing, S. Karunatillake, The Role of Ice and Latitude-Dependent Mantling on Boulder Distributions Across the Martian Northern Lowlands. *JGR Planets* **129**, e2024JE008387 (2024). <https://doi.org/10.1029/2024JE008387>
24. D. R. Hood, A. L. Cohen-Zada, R. C. Ewing, S. Karunatillake, Limits on polygonal organization of boulders in the Martian northern lowlands. *Icarus* **419**, 115850 (2024).
25. R. A. Beyer, O. Alexandrov, S. McMichael, The Ames Stereo Pipeline: NASA’s Open Source Software for Deriving and Processing Terrain Data. *Earth and Space Science* **5**, 537–548 (2018).
26. Q.-X. Liu, *et al.*, Phase separation explains a new class of self-organized spatial patterns in ecological systems. *Proc. Natl. Acad. Sci. U.S.A.* **110**, 11905–11910 (2013). <https://doi.org/10.1073/pnas.1222339110>
27. Q.-X. Liu, *et al.*, Phase separation driven by density-dependent movement: A novel mechanism for ecological patterns. *Physics of Life Reviews* **19**, 107–121 (2016).
28. X. Dong, D. D. Richter, A. Thompson, J. Wang, The primacy of temporal dynamics in driving spatial self-organization of soil iron redox patterns. *Proc. Natl. Acad. Sci. U.S.A.* **120**, e2313487120 (2023).
29. M. E. Cates, C. Nardini, Active phase separation: new phenomenology from non-equilibrium physics. *Rep. Prog. Phys.* **88**, 056601 (2025). DOI: 10.1088/1361-6633/add278
30. I. B. Smith, A. Spiga, J. W. Holt, Aeolian processes as drivers of landform evolution at the South Pole of Mars. *Geomorphology* **240**, 54–69 (2015).
31. T. A. Douglas, M. T. Mellon, Sublimation of terrestrial permafrost and the implications for ice-loss processes on Mars. *Nat Commun* **10**, 1716 (2019).
32. G. B. M. Pedersen, J. W. Head, Evidence of widespread degraded Amazonian-aged ice-rich deposits in the transition between Elysium Rise and Utopia Planitia, Mars: Guidelines for the recognition of degraded ice-rich materials. *Planetary and Space Science* **58**, 1953–1970 (2010).
33. C. M. Dundas, S. Byrne, A. S. McEwen, Modeling the development of martian sublimation thermokarst

landforms. *Icarus* **262**, 154–169 (2015).

34. L. Zhang, *et al.*, Buried palaeo-polygonal terrain detected underneath Utopia Planitia on Mars by the Zhurong radar. *Nat Astron* **8**, 69–76 (2023).
35. J. R. Zimbelman, S. M. Clifford, S. H. Williams, “Concentric Crater Fill on Mars: An Aeolian Alternative to Ice-rich Mass Wasting” in *Proceedings of the 19th Lunar and Planetary Science Conference*, (Lunar and Planetary Institute, Houston, TX, 1989), pp. 397-407.
36. G. A. Morgan, J. W. Head, D. R. Marchant, Lineated valley fill (LVF) and lobate debris aprons (LDA) in the Deuteronilus Mensae northern dichotomy boundary region, Mars: Constraints on the extent, age and episodicity of Amazonian glacial events. *Icarus* **202**, 22–38 (2009).
37. D. M. H. Baker, J. W. Head, D. R. Marchant, Flow patterns of lobate debris aprons and lineated valley fill north of Ismeniae Fossae, Mars: Evidence for extensive mid-latitude glaciation in the Late Amazonian. *Icarus* **207**, 186–209 (2010).
38. K. L. Tanaka, S. J. Robbins, C. M. Fortezzo, J. A. Skinner, T. M. Hare, The digital global geologic map of Mars: Chronostratigraphic ages, topographic and crater morphologic characteristics, and updated resurfacing history. *Planetary and Space Science* **95**, 11–24 (2014).
39. S. I. Outcalt, An Algorithm for Needle Ice Growth. *Water Resources Research* **7**, 394–400 (1971).
40. V. Meentemeyer, J. Zippin, Observations of Needle Ice Growth and Potential for Accelerated Erosion on the Georgia Piedmont. *Southeastern Geographer* **20**, 31–41 (1980).
41. D. M. Lawler, Environmental Limits of Needle Ice: A Global Survey. *Arctic and Alpine Research* **20**, 137–159 (1988).
42. A. W. Rempel, Formation of ice lenses and frost heave. *J. Geophys. Res.* **112**, 2006JF000525 (2007). doi:10.1029/2006JF000525, 2007
43. Z. Fu, Q. Wu, W. Zhang, H. He, L. Wang, Water Migration and Segregated Ice Formation in Frozen Ground: Current Advances and Future Perspectives. *Front. Earth Sci.* **10**, 826961 (2022).
44. J. R. Mackay, W. H. Mathews, Movement of Sorted Stripes, the Cinder Cone, Garibaldi Park, B. C., Canada. *Arctic and Alpine Research* **6**, 347–359 (1974).
45. I. Berthling, T. Eiken, J. L. Sollid, Frost Heave and Thaw Consolidation of Ploughing Boulders in a Mid-Alpine Environment, Finse, Southern Norway. *Permafrost & Periglacial* **12**, 165–177 (2001).
46. C. K. Ballantyne, Measurement and theory of ploughing boulder movement. *Permafrost & Periglacial* **12**, 267–288 (2001).
47. N. Matsuoka, M. Abe, M. Ijiri, Differential frost heave and sorted patterned ground: field measurements

and a laboratory experiment. *Geomorphology* **52**, 73–85 (2003).

- 48. A. Kääb, L. Girod, I. Berthling, Surface kinematics of periglacial sorted circles using structure-from-motion technology. *The Cryosphere* **8**, 1041–1056 (2014). <https://doi.org/10.5194/tc-8-1041-2014>
- 49. C. Yamagishi, N. Matsuoka, Laboratory frost sorting by needle ice: a pilot experiment on the effects of stone size and extent of surface stone cover. *Earth Surf. Process. Landforms* **40**, 502–511 (2015).
- 50. A. Li, N. Matsuoka, F. Niu, Frost sorting on slopes by needle ice: A laboratory simulation on the effect of slope gradient. *Earth Surf. Process. Landforms* **43**, 685–694 (2018).
- 51. A. R. Groos, *et al.*, The enigma of relict large sorted stone stripes in the tropical Ethiopian Highlands. *Earth Surf. Dynam.* **9**, 145–166 (2021).
- 52. C. Wang, *et al.*, Experimental and Modeling of Residual Deformation of Soil–Rock Mixture under Freeze–Thaw Cycles. *Applied Sciences* **12**, 8224 (2022).
- 53. N. Matsuoka, How can needle ice transport large stones? Twenty-one years of field observations. *Earth Surf. Process. Landforms* **48**, 3115–3127 (2023).
- 54. A. Kellerer-Pirklbauer, *et al.*, Acceleration and interannual variability of creep rates in mountain permafrost landforms (rock glacier velocities) in the European Alps in 1995–2022. *Environ. Res. Lett.* **19**, 034022 (2024).
- 55. T. L. Hudson, *et al.*, Water vapor diffusion in Mars subsurface environments. *J. Geophys. Res.* **112**, 2006JE002815 (2007).
- 56. P. H. Smith, *et al.*, H₂O at the Phoenix Landing Site. *Science* **325**, 58–61 (2009).
- 57. C. M. Dundas, *et al.*, HiRISE observations of new impact craters exposing Martian ground ice. *JGR Planets* **119**, 109–127 (2014).
- 58. A. M. Bramson, S. Byrne, J. Bapst, Preservation of Midlatitude Ice Sheets on Mars. *JGR Planets* **122**, 2250–2266 (2017).
- 59. C. M. Dundas, *et al.*, Exposed subsurface ice sheets in the Martian mid-latitudes. *Science* **359**, 199–201 (2018).
- 60. L. Fanara, K. Gwinner, E. Hauber, J. Oberst, Present-day erosion rate of north polar scarps on Mars due to active mass wasting. *Icarus* **342**, 113434 (2020). <https://doi.org/10.1016/j.icarus.2019.113434>
- 61. S. Diniega, *et al.*, Modern Mars’ geomorphological activity, driven by wind, frost, and gravity. *Geomorphology* **380**, 107627 (2021).
- 62. J. M. Moore, *et al.*, Sublimation as a landform-shaping process on Pluto. *Icarus* **287**, 320–333 (2017).

63. J. Laskar, *et al.*, Long term evolution and chaotic diffusion of the insolation quantities of Mars. *Icarus* **170**, 343–364 (2004).
64. D. E. Smith, *et al.*, Mars Orbiter Laser Altimeter: Experiment summary after the first year of global mapping of Mars. *J. Geophys. Res.* **106**, 23689–23722 (2001).
65. Hibbard, S. M., G. R. Osinski, E. Godin, A. Kukko, “Terrestrial brain terrain and the implications for Martian mid-latitudes,” in *Seventh International Conference on Mars Polar Science and Exploration*, Ushuaia, Tierra del Fuego, Argentina, (January 13–17, 2020), Abstract. #6023. <https://www.hou.usra.edu/meetings/marspolar2020/pdf/6023.pdf>.

Supporting Information

MBT's distribution and the relation with GLFs

Martian brain terrain (MBT) is a unique landform found on the surface of Mars. Statistical results show that MBTs are distributed in the mid-latitude regions of both the northern and southern hemispheres of Mars, exhibiting a clear hemispheric symmetry (*SI Appendix, Fig. S1A*). This symmetric distribution suggests that their formation is controlled by global climatic processes. Furthermore, we have compiled studies on the distribution of glacial-related landforms on Mars (GLFs, LVF, CCF, LDA). The results indicate a strong correlation between the distribution of these ice-related landforms and that of MBTs, with the densest concentration found in the northern part of the Arabia Terra region. This suggests that the formation of MBTs is likely related to shallow subsurface water-ice activity, and the northern Arabia Terra represents a key area for studying Martian brain terrain. Therefore, the complex brain-like textures (*SI Appendix, Figs. S1B-H*) record information about Martian climatic evolution and the history of shallow subsurface ice activity, serving as an important geological archive for interpreting the planet's paleoclimate history.

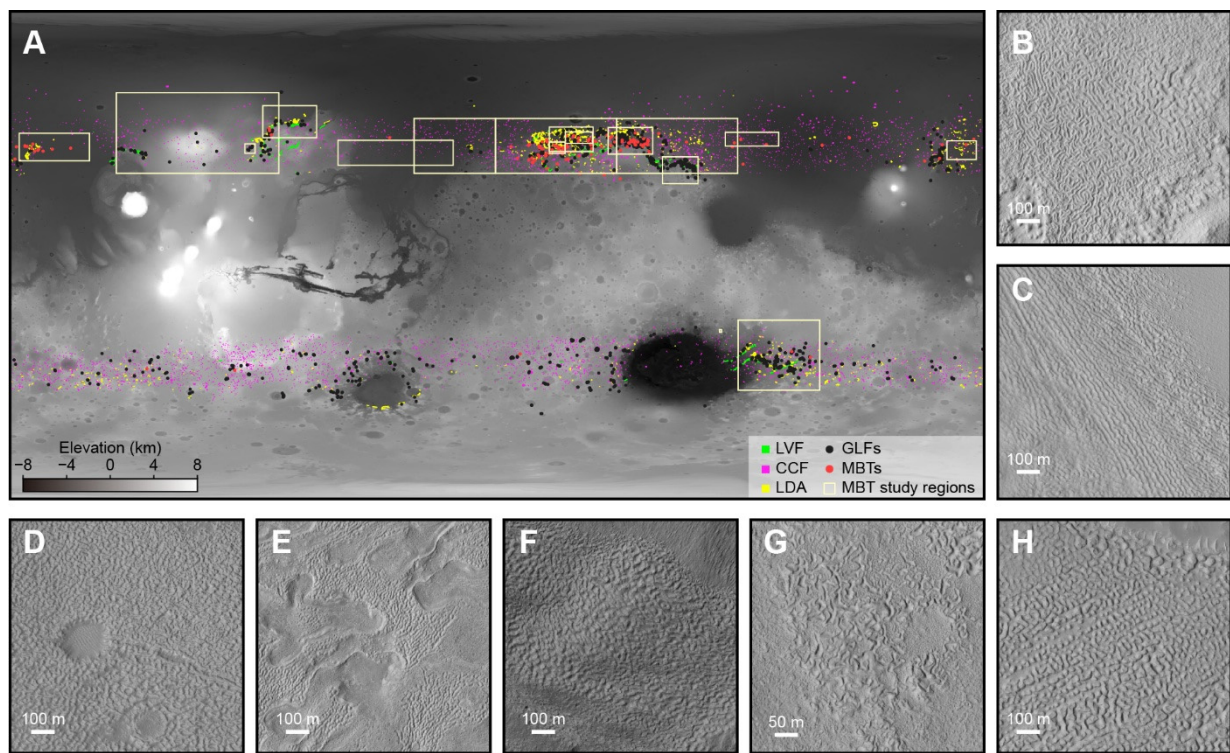


Fig. S1 Global distribution of MBT and related landforms. **A.** Distribution map, showing: MBTs (red dots (21)), GLFs (black dots (22)), and the LVF, CCF, and LDA (green, purple, and yellow areas, respectively (23)). Yellow squares indicate MBT study regions (4). **B-H.** are portions of HiRISE images, showing the surface morphology of MBT. Scale bars are located at the left bottom of each panel. The specific image IDs are: ESP_027521_2085_RED (28°N, 35.5°E), PSP_009588_2175_RED (37.3°N, 24.6°E), ESP_016155_2155_RED (35°N, 20.5°E), ESP_087641_2155_RED (35.2°N, 21.1°E), ESP_024380_1420_RED (37.7°S, 115.7°E), ESP_016782_2205_RED (40.1°N, 182.4°E), ESP_036615_2150_RED (34.8°N, 158°E). All HiRISE Images: NASA/JPL/University of Arizona.

Quantization system for extracting the morphological features of MBT

MBT Morphological Analysis. The Martian brain terrain (MBT) is a type of landform found on the Martian surface, characterized by its resemblance to the human brain. It primarily consists of sinuous ridges and grooves. Observations of

the study area reveal that the depressions within the MBT exhibit a distinct spatial progression in morphology (*SI Appendix*, Fig. S2A). This progressive variation is supported by both elevation data and contour maps (*SI Appendix*, Figs. S2B and C). Taking *SI Appendix*, Fig. S1A as an example, a clear spatial transition can be observed, where the depressions vary from simple, discrete bubble-like shapes to complex, continuous elongated strips along a specific direction.

Previous studies on the formation of MBT suggest that sublimation plays a significant role in its development, with sustained surface subsidence considered the primary formative process. Consequently, we suggest that the spatial sequence of the MBT is closely linked to the morphological characteristics and distribution of these depressions. Compared to the ridges, the morphology of the depressions provides more critical information for understanding the formation of MBT. Therefore, in this study, all geometric characterizations are focused on the morphology of depressions that constitute the MBT.

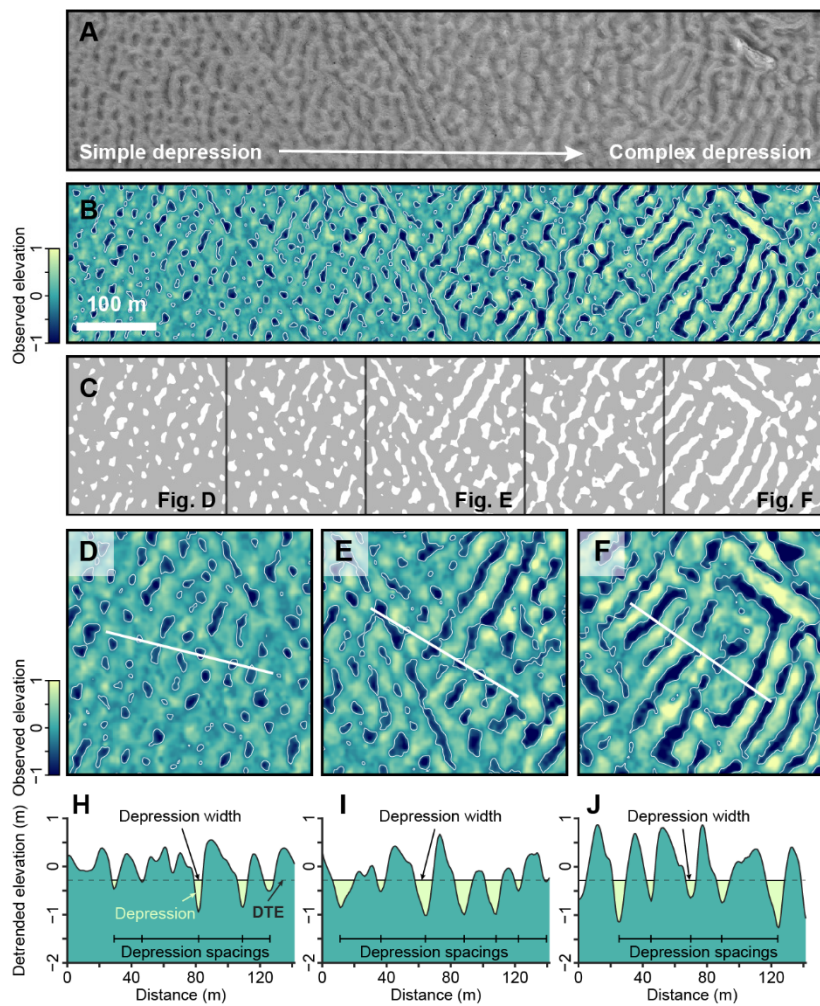


Fig. S2 Characterization of a local MBT in study area. **A. The HiRISE of local MBT in study area.** A continuous variation of depression from simple to complex is shown. **B. Corresponding processed elevation data of the same region.** The white contour lines represent the DTE = -0.2831 m. **C. The depression area map.** The area enclosed by the contour lines in (b) is filled with white color to highlight the depression areas. A-C share the same spatial scale; the scale bar is located at the left bottom of B. **D- F Detailed views of the grey rectangular area in (c),** showing the local topography at an enhanced scale. A white line in (D, E, F) marks the location of the topographic transect. **G-I. Elevation profiles along**

the transect line shown in D, E, F respectively. The definition of depression width and depression spacing are shown. The dash line represents the depression threshold elevation (DTE), the yellow region represents the depression.

Quantitative Geometric Characterization Metrics. Observations indicate that the spatial progression of MBT follows these trends: the depressions transition from a discrete to a dense distribution, increase in scale from small to large, and evolve in morphology from simple bubble-like shapes to sinuous elongated strips. To quantify this transition, we propose three metrics: Depression Area Fraction (DAF), Depression Spacing (DS), and Depression Width (DW). Their definitions are as follows:

(1) Depression Area Fraction: DAF is defined as the ratio of the area with an elevation below the Depression Threshold Elevation (DTE) to the total area within a specific region. It is expressed as:

$$\text{DAF} = \frac{S_{\text{depression}}}{S_{\text{region}}}$$

where $S_{\text{depression}}$ and S_{region} denote the area of the depressions and the total area of the region, respectively. This metric reflects the spatial distribution density of depressions. A high DAF value indicates a high density of depressions within the region (e.g., as observed in areas of complex morphology). In this study, we employed a simple depression-identification criterion: pixels with elevations below a given DTE are classified as part of a depression. Consequently, the calculated DAF value depends on the chosen DTE. For the observed MBT, a DTE value of -0.2831 m was applied (the rationale for this specific value is discussed in the section).

(2) Depression Spacing: DS describes the degree of dispersion of depressions within a region. It is a statistical metric representing a regional characteristic. Its derivation relies on calculating the horizontal distances between the lowest points of adjacent depressions within a defined area, followed by statistical analysis. The DS value thus quantifies the spatial separation of depressions.

(3) Depression Width: Similar to DS, DW is a statistical result representing the average size of depressions within a region. When depressions are regularly bubble-shaped, a larger DW corresponds to a greater average diameter. (The detailed extraction methodologies for DS and DW are presented in the next section).

In this study, DS and DW reflect the average characteristics of depressions within a given analysis window, rather than describing individual features. We provide their preliminary geometric definitions below. For a topographic profile across the study area, we first determine if it intersects depressions (i.e., if any segment has an elevation below the DTE). For profiles that do intersect depressions, the following calculations are performed:

1. Extract all local minimum points within the depression segments. The horizontal distances between successive minima are calculated, generating a set of depression spacing samples (DS_i). 2. Identify the intersection points where the profile elevation equals the DTE. The horizontal distance between two consecutive intersection points bounding a depression is defined as the width of that depression (DW_j). 3. Finally, statistical analysis is performed on all collected DS_i and DW_j samples to obtain the final representative DS and DW values for the region. Collectively, the parameters DAF, DS, and DW provide an accurate quantitative characterization of the geometric morphology of MBT depressions, establishing a basis for subsequent numerical modeling.

Quantitative Feature Extraction

Preprocessing of Elevation Data. The original elevation data used in this study were sourced from a Digital Terrain Model (DTM) dataset (DTEEC_033165_2195_032875_2195_A01 (1)). A prominent mountain with a height of ~800 m exists on the left side of this region (*SI Appendix*, Fig. S3A), introducing a significant large-scale background topographic trend across the study area. In the previous section, we introduced the preliminary definitions of the morphological characteristic parameters. It is evident that such a large-scale background trend would adversely affect our extraction results. To mitigate the influence of the large-scale trend and better highlight the small-scale features of the MBT, we first preprocessed the elevation data. The processing workflow is as follows: **1.** First, the study area was divided into a series of regular grids, with each sub-region sized 200 m × 200 m. For each sub-region, the arithmetic mean of all elevation points within it was calculated to obtain the local mean elevation (*SI Appendix*, Fig. S3B). This result can be regarded as a discrete representation of the large-scale topographic trend in the study area, which is used in the subsequent step to remove the background terrain signal. **2.** Next, the value of each pixel in the original elevation data was subtracted by the local mean elevation of its corresponding sub-region. This yielded the mean-removed elevation data (*SI Appendix*, Fig. S3C). This process can be expressed as:

$$h_{detrend}(x, y) = h_{raw}(x, y) - \bar{h}_{region}(x, y)$$

where $h_{detrend}(x, y)$ represents the detrended elevation, $h_{raw}(x, y)$ denotes the original elevation data, and $\bar{h}_{region}(x, y)$ signifies the local mean elevation. Subtracting the regional mean elevation preliminarily removes the large-scale background trend. **3.** As the regional subdivision may introduce artificial elevation discontinuities at sub-region boundaries (*SI Appendix*, Fig. S3C), Gaussian filtering was further applied to the detrended data to suppress such boundary effects. The filter kernel size was set to 21 with a standard deviation of 1. This step aims to smooth transitional discontinuities between sub-regions while preserving local topographic details. The smoothed data effectively mitigates the influence of the background trend, making the morphological features of the MBT more prominent, thereby providing a robust foundation for subsequent geometric feature extraction and analysis. **4.** Finally, we obtained the preprocessed elevation data, which had undergone both background trend removal and Gaussian smoothing (*SI Appendix*, Fig. S3D). All subsequent geometric feature extraction and the presented local elevation maps are based on this processed elevation data.

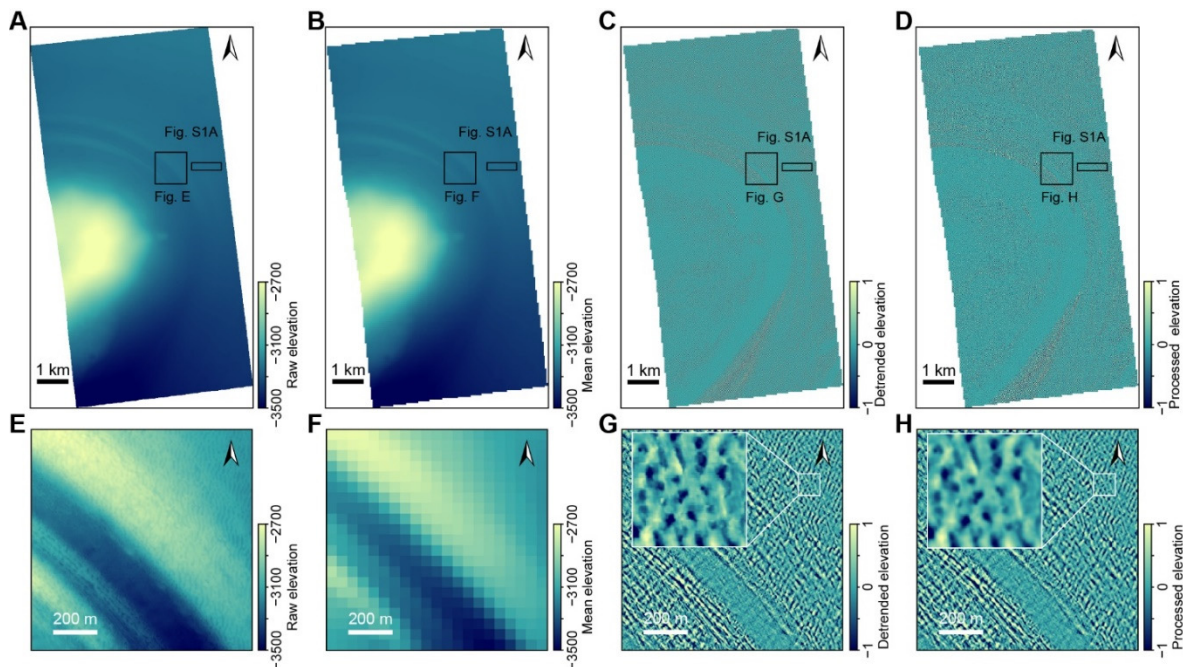


Fig. S3 Workflow for preprocessing topographic data in the study region. **A.** The visualization result of raw elevation data. **B.** Regional mean elevation, calculated within defined sub-regions, representing the background trend field. **C.** Detrended elevation data after removal of the regional mean and subsequent filtering to smooth boundary artifacts. **D.** Processed elevation data after Gaussian filtering. **E-H.** Zoom-in views of the area marked by the black rectangle in A-D. These detailed views highlight the preservation and modification of local topographic features through the background trend removal and smoothing process. Scale bars for the overview and the detailed panels are provided at the left bottom.

Geometric Parameter Extraction Workflow. Following the acquisition of the background-trend-removed elevation dataset, we proceeded to extract the quantitative morphological parameters (DAF, DW, DS) for the MBT. Among the morphological parameters, DAF can be directly obtained through regional tiling and a straightforward calculation. As defined in this study, the extraction of depression spacing and width is associated with profiles. Therefore, we first developed a rotation-slicing method to acquire profiles at various orientations across the study area.

Rotation-Slicing Method. The workflow to Rotation-Slicing Method obtaining these multi-directional profiles is as follows: (1) Construct an inscribed circle within a selected square region of interest. (2) Inside this circle, inscribe a square and designate it as the profile-sampling area. (3) Within this inscribed square, arrange a series of parallel profiles at a fixed interval to acquire profile data (*SI Appendix, Fig. S4A*). (4) For each profile, calculate the corresponding depression spacings (DS_i) and widths (DW_j) sample data according to the definitions provided in next section (*SI Appendix, Fig. S4B*). (5) Upon completing data extraction from all profiles at the current orientation, rotate the rectangular (inscribed square) sampling area. Use this rotated area as the new profile-sampling region, and repeat steps (3), (4), and (5) until the cumulative rotation angle reaches 180°.

Through this procedure, we obtained profile data from various orientations across the study area and extracted the corresponding depression spacing and width data from each profile. Finally, we performed statistical analysis on all collected DS_i and DW_j samples by calculating their arithmetic mean, thereby deriving the representative regional DW and DS values (*SI Appendix, Figs. S4C and D*).

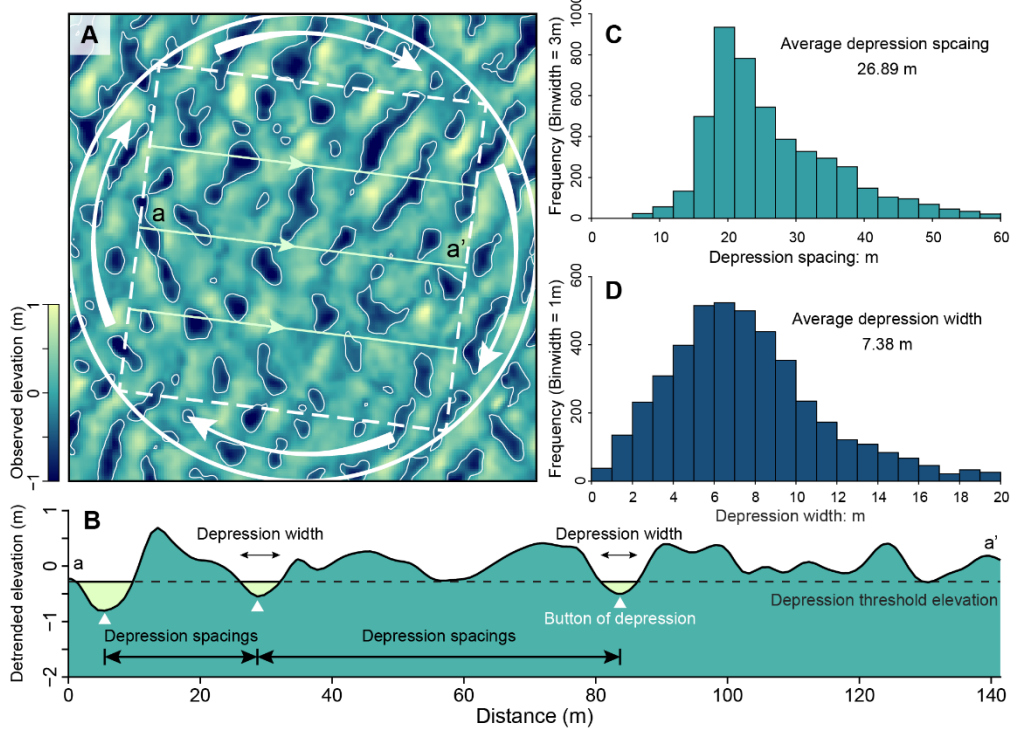


Fig. S4 Schematic diagram of morphological parameters extraction method flow. **A.** Schematic diagram of tangent selection method. The white circle represents the rotation range of inscribed rectangle. The dash lined rectangle represents the cutting area. The yellow lines represent the cutting lines and the arrows represent the cutting direction. **B.** Extraction of Geometric Features for Tangents. Yellow areas present the depression. The dash line is the Depression threshold elevation. The lines with arrows indicate DS and DW. **C-D.** The histograms of extracted DS and DW data.

Preliminary Screening of Extraction Results. Using the rotation-slicing extraction method proposed in the previous section, we obtained the spatial distribution of MBT morphological characteristics across the study area. However, it should be noted that, as mentioned, a prominent mountain exists within the study area where no MBT has developed (*SI Appendix*, Fig. S5A). Nevertheless, minor undulations on the surface of MBT-free area can still yield morphological parameter values during the extraction process (*SI Appendix*, Fig. S5B). The inclusion of these data would introduce unnecessary errors into subsequent analyses. Therefore, it is necessary to exclude these regions. Based on elevation data, surface roughness, and slope data, combined with manual identification, we masked these MBT-free regions (*SI Appendix*, Fig. S5C) to facilitate subsequent quantitative analysis.

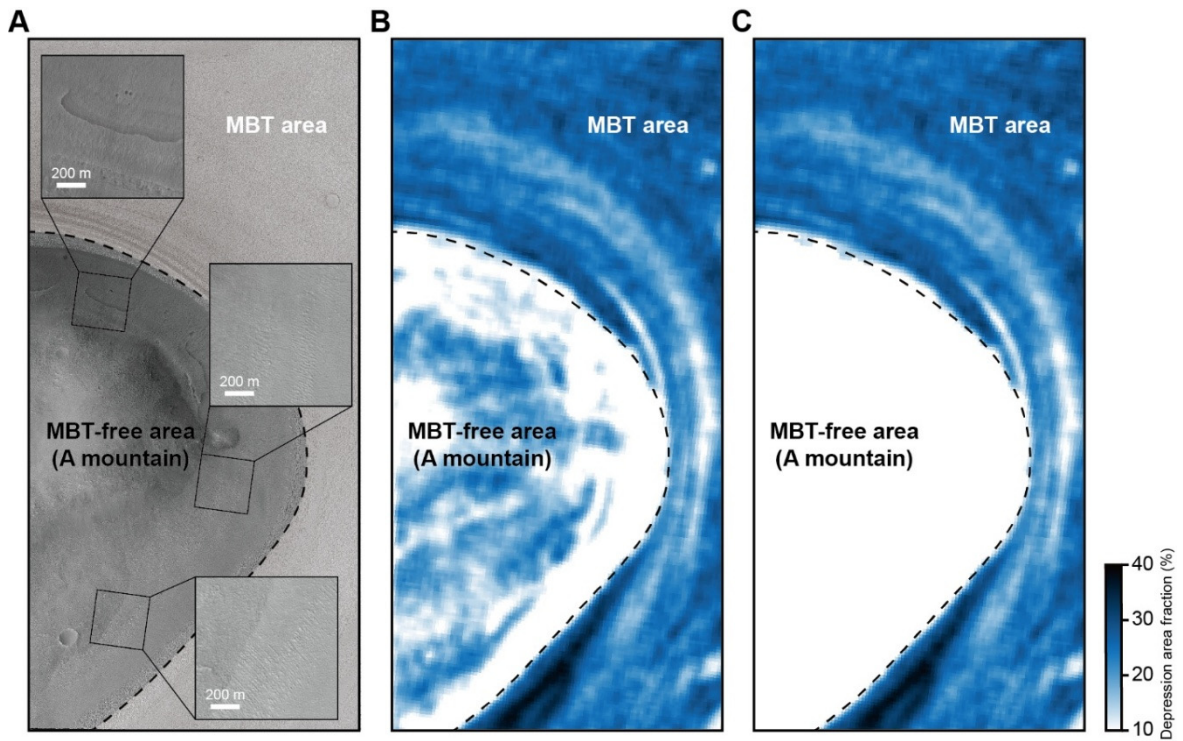


Fig. S5 Visualization of extraction results and preliminary exclusion of areas without MBT. **A.** The HiRISE imaging of study area. The dash line represents the boundary of MBT area and MBT-free area. Three enlarged partial images of MBT-free areas are displayed. **B-C.** The visualizations of raw extraction results and the result excluding the MBT-free area. The dashed lines represent the boundary line that is consistent with **A**. **B-C.** share a same color bar which is shown on the right bottom of **C**.

Quantitative Analysis of Extracted Geometric Features. Observations of the MBT within the study area reveal a spatial progression of depression morphology from simple to complex forms (*SI Appendix*, Figs. S2A-C). This progression can be quantitatively described using our proposed morphological parameters, primarily corresponding to a gradual increase in the Depression Area Fraction (DAF). In the prevailing genetic model for MBT, sublimation-induced surface erosion is considered the primary process shaping its geometry. From the perspective of MBT formation via surface erosion, different depression morphologies may indicate varying degrees of MBT development. Furthermore, the numerical simulations conducted in this study demonstrate that, within a self-organization framework, the emergence of patterns with a high DAF requires a longer evolution timescale. Therefore, we propose that the DAF of MBT reflects its developmental degree, where a higher DAF corresponds to a more advanced stage of MBT development. Based on this proposition, we constructed DAF-DS and DAF-DW diagrams to investigate the variation patterns of the DS and DW parameters across different developmental stages of MBT.

Local Aggregation Statistics Based on a Moving Window. To investigate the systematic relationships between DAF and the DW/DS parameters, and to quantify their variation trends along with associated uncertainties, we performed local aggregation statistics based on a moving window on the DAF-DS and DAF-DW scatter plot data. The specific processing workflow is as follows: **1.** Data Binning: Using DAF as the independent variable, a series of consecutive windows of equal width (window width: 3%) were defined along the DAF axis. Each window covers a specific interval of DAF values. **2.** Within-bin Statistics: For all data points falling within each window, their arithmetic mean and standard deviation (SD) were calculated. **3.** Trend Line and Error Visualization: The mean values computed for each window were plotted on a

scatter diagrams. Connecting these points formed the mean trend lines for DAF-DS and DAF-DW relationships (*SI Appendix, Figs. S6A and B*). Simultaneously, the dispersion of the average DW and DS results within each window was visualized using error bars, representing the uncertainty of the data around the trend lines.

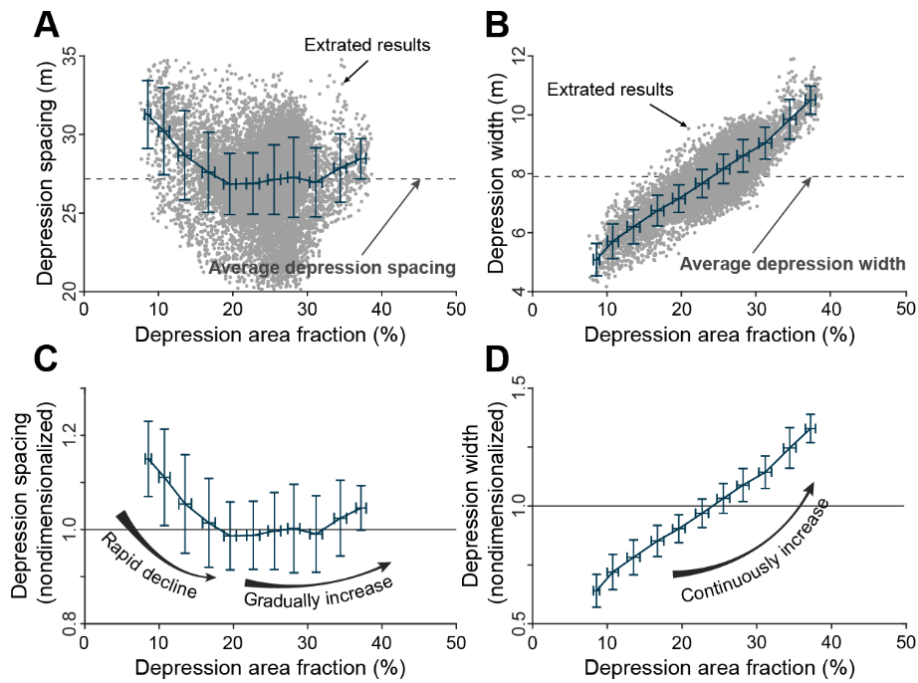


Fig. S6 Extraction results of MBT's morphological parameters. A-B The raw extraction results and statistic results of DS and DW in study area. The grey dots are the sample data and the dash lines A and B represent average depression spacing and depression width in study area respectively. The error bars denote the standard deviation. **C-D The results after the nondimensionalization.** The black line represents the average values. The shaded regions denote the standard deviation.

Dimensional Normalization of Data Results. After obtaining the mean trend lines for DAF-DS and DAF-DW (*SI Appendix, Figs. S6A and B*), dimensional normalization was applied to both trend lines to eliminate scale effects and establish direct comparability between the observational data and subsequent numerical simulation results. The specific methodology is as follows: for the DAF parameter, which is inherently a dimensionless ratio, the original values were retained. For the parameters DS and DW, which possess dimensions of length, a global mean normalization method was employed. This involved calculating the arithmetic means of all DS and DW sample points across the entire study area, respectively, and then dividing each original sample value by its corresponding global mean. Within the study area, the average DS of the MBT is 27.1811 ± 2.3208 m, and the average DW is 7.8974 ± 0.92556 m. The results after dimensional normalization are shown in *SI Appendix, Figs. 6C and D*.

Systematic Relationships Between Depression Area Fraction, Spacing, and Width. Following local aggregation statistics based on a moving window and subsequent dimensional normalization, we established the quantitative relationships between the Depression Area Fraction (DAF) and both the Depression Spacing (DS) and Depression Width (DW) of the MBT (*SI Appendix, Figs. S6C and D*). Analysis of the results reveals that as DAF increases, the depression spacing shows an initial rapid decrease followed by a gradual increase. The inflection point occurs at approximately DAF $\sim 20\%$. In contrast, the depression width exhibits a positive correlation with the depression area fraction. These variation trends provide a crucial basis for comparison with subsequent numerical simulation results.

Numerical Modeling: A Self-Organization-Driven Transport Model

Research on the Genetic Mechanisms of MBT. The formation of MBT likely involves complex processes, including wind action, glaciation, freeze-thaw cycles, thermal cracking (2). The prevailing view suggests that MBT formation involves thermal cracking processes followed by continuous modification through sublimation (3). Studies of analogous terrestrial landforms also propose that aeolian processes may play a role in MBT formation (4). Recently, the discovery of self-organized patterned ground on Earth, morphologically similar to MBT, has provided a new perspective on its genesis. The hypothesis of self-organized stone transport as a cause for MBT has begun to gain attention. Several numerical simulation studies have been conducted on Earth to replicate the formation of these self-organized landforms (5, 6). Based on extensive observational constraints, [Kessler et al., \(2001\)](#) developed a self-organization model simulating the mutual pushing and transport of stones during freeze-thaw cycles, successfully reproducing the geometric patterns of patterned ground. [Li et al., \(2021\)](#) through laboratory experiments, replicated the self-organized stone transport process during freeze-thaw cycles, further substantiating the self-organization-driven transport mode of stones under cyclic freezing and thawing. However, due to the scarcity of *in-situ* observational data from Mars, which leads to a lack of constraints for models, numerical simulation studies specifically targeting the self-organization genesis of MBT have not yet been undertaken.

Dynamic Model of Self-Organized Clast Transport

Phase Separation Theory and Physical Context. Phase separation has emerged in recent years as a key physical principle for describing self-organization processes and has been applied to research in numerous fields, including self-organized landforms (5–8). In this study, we construct a self-organization dynamic model based on the theory of phase separation to describe the transport process of stones under the influence of freeze-thaw cycles, and employ it to investigate the self-organization genesis of MBT.

First, we establish the following physical context: Initially, stones of uniform size are evenly distributed on the surface of water-bearing soil. Under the influence of freeze-thaw cycles, water within the soil migrates and transitions from a liquid to a solid state. During ice formation, the associated volume change exerts pressure on the surface stones, inducing displacement. In addition to water migration and phase change, the growth of needle ice beneath the stone also contributes to their transport (6, 9, 10). Existing laboratory experimental data indicate that under these conditions, the transport process of a clast is influenced by the local concentration of surrounding stones (6). Transport rates are lower in areas of high stone concentration and higher in areas of low stone concentration.

This differential in transport velocity establishes a positive feedback mechanism: the low transport rate in dense zones hinders stones from migrating out into sparse zones, while the high transport rate in sparse zones facilitates a net macroscopic transport of stones from sparse zones towards dense zones. This further reduces the stone density in the original sparse zones and accelerates their segregation. Driven by this feedback, stones spontaneously begin to aggregate, forming regular zones of high and low concentration, which manifest as a regular pattern.

Meanwhile, the stone concentration cannot increase indefinitely. When it reaches a certain threshold (forming clast piles), constraints from inter-clast mechanical properties and gravity cause the piles to collapse, leading to a decrease in local clast concentration. This constitutes a macroscopic negative feedback mechanism. Under the combined action of these two feedback mechanisms, and after a sufficient number of freeze-thaw cycles, the system evolves toward a stable configuration

with distinct stone-dense zones and stone-sparse zones, ultimately form stable self-organized patterns (e.g., polygons, labyrinths, and brain-like pattern).

The physical feedback mechanisms described above provide a qualitative understanding of self-organization. To integrate these mechanisms into a unified, mathematically tractable framework for quantitative exploration, we note a profound macroscopic analogy between stone transport and diffusion process. Both processes are driven by density gradients and are capable of producing ordered patterns through positive feedback. This conceptual parallel allows us to construct a model by generalizing the well-established mathematics of diffusion.

Generalized Fick's Law. Fick's law is the classical diffusion theory and it describes the transport of particles driven by thermal motion from areas of high concentration to areas of low concentration. Although the mechanism of frost-driven stone movement is fundamentally different from molecular thermal motion, both macroscopically exhibit the common feature of "redistribution of material from high-density to low-density zones" and, under certain conditions, can lead to ordered phase separation through similar positive feedback mechanisms. Therefore, we adopt an analog modeling strategy: by drawing on the well-established mathematical formalism used to describe random walks (the microscopic basis of diffusion), we reinterpret its variables in accordance with the physical essence of our system, thereby constructing a self-organization model suitable for qualitative and semi-quantitative analysis.

Analogy Between Self-Organized Clast Transport and a Random Walk Model. To incorporate the transport process of stones driven by freeze-thaw cycles into a mathematical framework amenable to stability analysis and pattern prediction, we draw an equivalence between its macroscopic, long-term statistical behavior and a generalized "effective random walk" process. It is crucial to note that this analogy does not imply identical microscopic mechanisms, but is justified because both systems, when sharing the following key characteristics, obey similar continuum macroscopic equations: (1) Discreteness and Periodicity of Displacement: In our constructed physical scenario, stone movement is not continuous but driven by discrete freeze-thaw events. Each displacement event can be regarded as a "step" in a random walk model. (2) Randomness in Displacement Direction: The displacement of a clast during a freeze-thaw cycle is influenced by micro-topographic variations, the growth of underlying needle ice, collisions with neighboring clasts and some other random processes. Therefore, we consider the direction of stone movement to be random during a freeze-thaw event. (3) Density Dependence of Displacement Magnitude: This is the core physical input of our model to explain the forming of brain-like pattern. Theoretical analysis suggests that the effective displacement of a stone declines as the local stone density increases. This negative correlation between stone transport rate and local stone concentration has also been observed in actual laboratory experiments and its expression is (9):

$$v(c) = v_{max} \cdot e^{-\lambda c}$$

Here, v_{max} is the maximum transport rate of a stone, whose physical meaning is the displacement of an isolated stone during a single freeze-thaw cycle. λ is the rate decay coefficient, representing how rapidly the stone's transport rate decreases with increasing concentration. It should be noted that, since we set the model's timestep to correspond to one freeze-thaw cycle, the velocity (v) here has a temporal unit of per cycle, rather than a conventional continuous-time unit. Referring to the experimental data from [Li et al., \(2021\)](#) and *in-situ* observational results, under given experimental conditions, the displacement of a stone per freeze-thaw cycle is on the order of millimeters.

Redefinition of Variables. Here, we employed the generalized Fick's law derived by [Schnitzer \(1993\)](#)(11) for spatially dependent random walks to draw an analogy with the self-organized transport process of stones. Within the theoretical framework proposed by Schnitzer, the variables need to be redefined as follows:

(1) Effective Step Length and Effective Stone Transport Rate: We reinterpret the constant speed in the random walk model as a position-dependent quantity representing the displacement a stone acquires during a single freeze-thaw cycle. Its spatial dependence is entirely determined by the local stone concentration. Furthermore, we treat one freeze-thaw cycle as one timestep, focusing only on the distribution of stones after an integer number of complete cycles.

(2) Particle Collision Rate (α): In the random walk model, α describes the frequency of particle collisions. In our conceptual model, we treat α as a comprehensive effective parameter that quantifies the overall rate at which various stochastic factors (e.g., micro-topography, collisions) cause the decay of directional memory in stone movement. To focus on the core feedback mechanism $v(c)$, we set α as a constant in this preliminary exploration.

(3) Effective Diffusion Coefficient: In random walk theory, the diffusion coefficient is given by $D(c) = \frac{-v^2(c)}{d\alpha}$, where d is the spatial dimension. This relation connects microscopic motility parameters to macroscopic diffusive strength. We adopt this relationship as the effective definition for our model, as it quantifies the macroscopic transport capacity exhibited by stone movement at a specific local density.

(4) Gradient Energy Coefficient (κ): To describe the finite-width transition zone between stone-dense and stone-sparse regions after phase separation, we introduce the standard gradient energy term from the Cahn-Hilliard equation, $-\kappa\nabla^2 c$. This term represents interactions within the stone collective, such as geometric exclusion due to impenetrability, friction, and stability constraints imposed by gravity. It penalizes overly sharp concentration interfaces and governs the characteristic spatial scale of the self-organized patterns.

Dynamic Model Construction. Building upon the analogy and reinterpretation, we take the generalized flux form derived by [Schnitzer \(1993\)](#) for spatially dependent random walks as our starting point. When the particle collision rate α is constant and the velocity $v(c)$ varies with concentration, the mass flux of stones, J_{cv} , is given by:

$$J_{cv} = -D(c)\nabla c - \frac{c(r)}{2}D'(c)$$

This flux expression indicates that the stone flux is driven not only by the concentration gradient, i.e., $-D(c)\nabla c$, but also by the gradient of the transport capacity itself, i.e., $-\frac{c(r)}{2}D'(c)$, where $D'(c)$ denotes the derivative of the diffusion coefficient with respect to concentration. Here, $D(c) = \frac{-v^2(c)}{d\alpha}$, with d representing the spatial dimensionality. The first term in this expression is the Fickian diffusion term, and the second term is a drift term arising from the gradient of the diffusion coefficient. In the context of our model, the physical interpretation of this flux is the macro-scale mass flow of stones induced by freeze-thaw cycles and modulated by the local concentration. Substituting the flux J_{cv} into the mass conservation equation $\frac{\partial \rho}{\partial t} = -\nabla J_{cv}$, we obtain:

$$\frac{\partial c}{\partial t} = \nabla \cdot \left(D(c)\nabla c + \frac{c(r)}{2}D'(c) \right)$$

Here, we construct $G(\mathbf{r})$ such that $\nabla G(c) = D(c)\nabla c + \frac{c(\mathbf{r})}{2}D'(c)$, which transforms the equation above into:

$$\frac{\partial c}{\partial t} = \nabla^2(G(c))$$

Subsequently, by introducing the gradient term $-\kappa\nabla^2 c$ representing interfacial energy, we arrive at the final kinetic equation based on phase separation:

$$\frac{\partial c}{\partial t} = \nabla^2(G(c) - \kappa\nabla^2 c)$$

Unified Framework of Phase Separation Theory. Ultimately, the equation we obtain is mathematically identical in form to the classical Cahn-Hilliard equation:

$$\frac{\partial c}{\partial t} = M\nabla^2 \left(\frac{\partial f}{\partial c} - \kappa\nabla^2 c \right)$$

The Cahn-Hilliard equation is a universal model describing phase separation driven by a density-dependent chemical potential. In this work, $G(c)$ plays a role analogous to the chemical potential $\frac{\partial f}{\partial c}$ in the Cahn-Hilliard equation, with its specific form determined by $D(c)$ and $v(c)$. Consequently, although the starting point of our model's derivation is a mathematical analogy to random walk theory, its final form successfully maps its physical core onto the theoretical framework of phase separation. This allows us to directly leverage the established results from this framework to analyze the growth of phase-separation patterns.

Model Parameter Calibration

Initial Stone Concentration and Rate Decay Coefficient. This model requires the initial stone concentration as an input condition. The lack of *in-situ* observational data makes it difficult to provide direct constraints. Therefore, we utilize Orbital observation data of the study area to constrain the initial stone concentration. Rock abundance data derived from Mars Viking IRTM (Infrared Thermal Mapper) measurements indicate that the rock abundance in the Arabia Terra region is $5.6\% \pm 1.8\%$ (12). Rock abundance refers to the ratio of the projected area of rocks to the total area per unit area. Based on the rock abundance-particle size relationship curve proposed by M. Golombek and D. Rapp, we can derive the theoretical stone diameter distribution curve for the study area (*SI Appendix*, Figs. S7A and B). Through a simple calculation, we can estimate that, given a stone density of 2500kg/m^3 and the shape of stone varies from stander circle to elliptical ($e = 1.0 - 2.0$), a rock abundance of 3.8-7.4% roughly corresponds to a stone concentration of about 15 kg/m^2 to 45 kg/m^2 (*SI Appendix*, Fig. S7C). This provides a constraint on the present-day surface stone concentration on Mars.

Our model follows the principle of mass conservation, implying that the total mass of stones remains constant before and after the self-organization process. Therefore, we assume that during the evolution of the MBT, stones were merely transported and not weathered away, leading to no net mass loss. Based on this assumption, we propose that the stone concentration at the initial stage of MBT formation in the study area was consistent with the presently observed value, i.e., 15 kg/m^2 to 45 kg/m^2 . Considering that stone concentration is not the core focus parameter of this study, we select a value of 30 kg/m^2 as the initial concentration for model input. During the simulation process, we introduced some slight random perturbations to simulate the initial distribution of the stone.

In this model, the rate decay coefficient (λ) characterizes how rapidly the stone transport rate decreases with increasing local concentration. Its value is derived from experimental fitting results. Li et al., (2021) conducted extensive statistical analysis of laboratory data and found that the system behavior bifurcates when λ is set to 3.0 and 0.85. In order to confirm the impact of λ and initial stone concentration on the phase separation mode, we conducted a parameter scan (*SI Appendix*, Fig. S8) where the λ range from 0.5 to 1.5 and the initial stone concentration from 1 to 71 kg/m². The results indicate that when the initial particle concentration is set at 30 kg/m², the required λ value for phase separation is approximately less than 1.1. Considering the low-gravity environment on Mars, the gravitational drag force on stones during transport is likely reduced, which may partially weaken the inhibitory effect of stone concentration on transport rate. Therefore, this model primarily adopts a scenario of slowly decaying transport rate, corresponding to $\lambda = 0.85$.

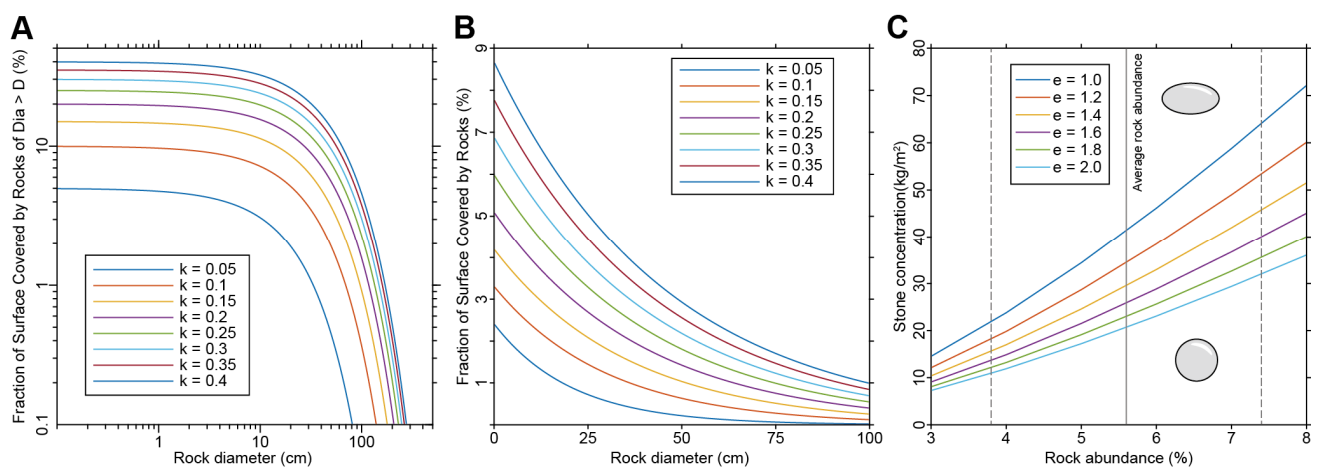


Fig. S7 Calibration of initial stone concentration. **A.** Rock abundance-particle size relationship, described by the function $F(D) = a \cdot e^{(-b \cdot D)}$, where $a=0.176$, $b=2.73(24)$. In the figure, k denotes rock abundance. **B.** Derived particle size and corresponding coverage curve for stones, derived from A. **C.** Rock abundance-stone concentration curve below stones. e denotes the eccentricity of stones.

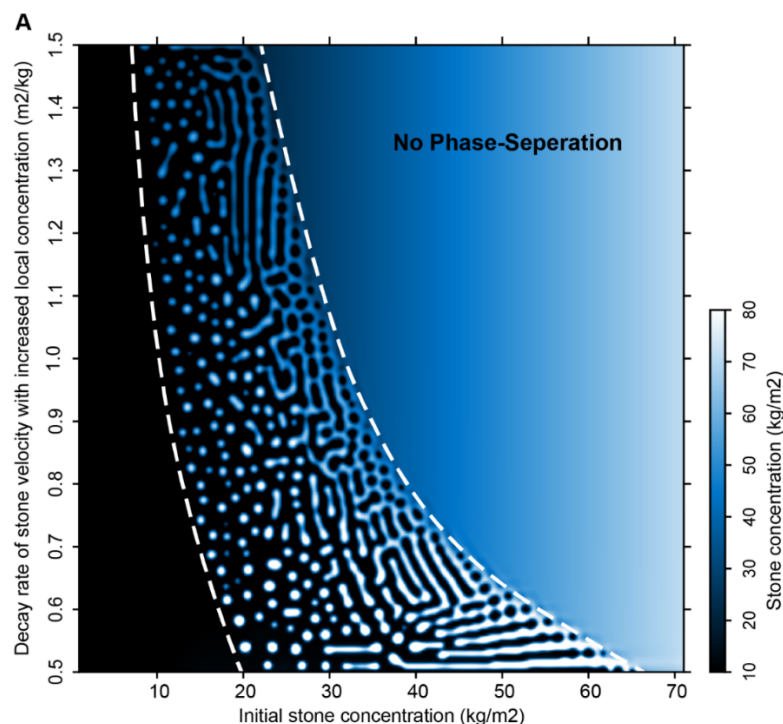


Fig. S8 Results of the parametric scan. This figure presents simulation results under varying initial stone concentrations (1-71 kg/m²) and λ (0.5-1.5 m²/kg). The domain size is 1024 m × 1024 m, the simulation was run for 10¹⁰ steps, with $v_{max} = 3$ mm/cycle and $\kappa = 0.225$. The color bar is shown on the right bottom of the figure. The white dashed line represents the boundary where phase separation occurs.

Selection of Total Simulation Steps. In this model, the choice of total simulation steps directly determines whether a distinct phase separation process can be observed. Previous simulations of centimeter-scale stone transport processes indicate that significant phase separation emerges at approximately 10⁴ steps. However, the spatial scale of our model is 200 m × 200 m. Assuming a linear scaling relationship with simulation steps, observing significant phase separation in our modeling scale would require on the order of 10⁸⁻⁹ steps. Considering that this scaling may be nonlinear, and that larger spatial scales might require more steps for pronounced phase separation to occur, we initially tested results for 10⁸ to 10¹⁰ steps. The results indicate that the phase separation process generally begins to manifest around 2×10⁹ steps.

Calibration of the κ Value. In this model, the higher-order gradient term $-\kappa\nabla^2c$ prevents the formation of overly sharp interfaces, constraining the thickness of the phase boundary. Here, it specifically constrains the minimum scale of the brain-like patterns. Describing this from the perspective of the morphological characteristic parameters defined in this study, the κ value governs the minimum depression spacing (DS) that emerges during the phase separation process (in the geometric analysis of phase-separation patterns, we refer to the time point when this minimum depression spacing appears as the transition point). Through a parametric scan, we analyzed the minimum achievable depression spacing during phase separation for different κ values in the range between 0.05 and 0.30 (*SI Appendix*, Figs. S9A-F). The results show that when κ is 0.20 and 0.25, the calculated minimum depression spacings are 25.07 m and 27.27 m, respectively. Concurrently, the average value of samples within the minimum depression spacing interval for the MBT in the study area is 26.76 m (*SI Appendix*, Figs. S8G-I). Therefore, we selected an intermediate value 0.225 as the κ value input to the model.

Table S1. Definitions and interpretation of variables and parameters in dynamic model

Symbol	Value	Unit	Definition and Interpretation
$c_{initial}$	30	kg/m ²	Initial stone concentration
λ	0.85	m ² /kg	Decay rate of stone velocity with increased local concentration
α	1	1/cycle	Particle Collision Rate
κ	0.225	-	Coefficient of gradient energy controlling the width of transition regions between two phases

Analysis of Temporal Evolution Characteristics in Phase Separation. In the preceding sections, we have established the quantitative characteristic parameters for MBT and formulated the dynamic model describing the self-organization-driven transport process of stones. Our next objective is to perform geometric feature extraction on the simulation results as well. This will allow us to quantitatively investigate the correlation between the patterns formed by the self-organized stone transport process and the morphological characteristics of MBT, thereby providing a basis for discussing the plausibility of the self-organization genesis mechanism for MBT.

Quantitative Analysis of the Phase Separation Temporal Process Based on Geometric Features. First, we conducted a quantitative analysis of the evolutionary progression of the self-organized patterns. We simulated the self-organization process for 3×10⁹ steps. For the output at each simulated time point, we extracted the morphological characteristic

parameters DAF and DS, obtaining the evolution curves of DAF and DS for the self-organized patterns (*SI Appendix*, Figs. S10A and B). The results reveal that as the simulation steps increase, the DAF gradually rises, indicating an expansion of the depressed regions. This increase is not linear: it occurs rapidly during a relatively short period (between about 2×10^9 and 3×10^9 steps) and then gradually slows down. Regarding the DS, a more complex trend is observed. In the early stages of pattern development, the DS is relatively large representing a discrete distribution of depressions (*SI Appendix*, Fig. S10C). Subsequently, as the simulation steps advance, the DS initially undergoes a rapid decrease, reaching a minimum around 3.0×10^9 steps (*SI Appendix*, Fig. S10D). Following this point, the DS slowly increases with further steps (*SI Appendix*, Fig. S10E).

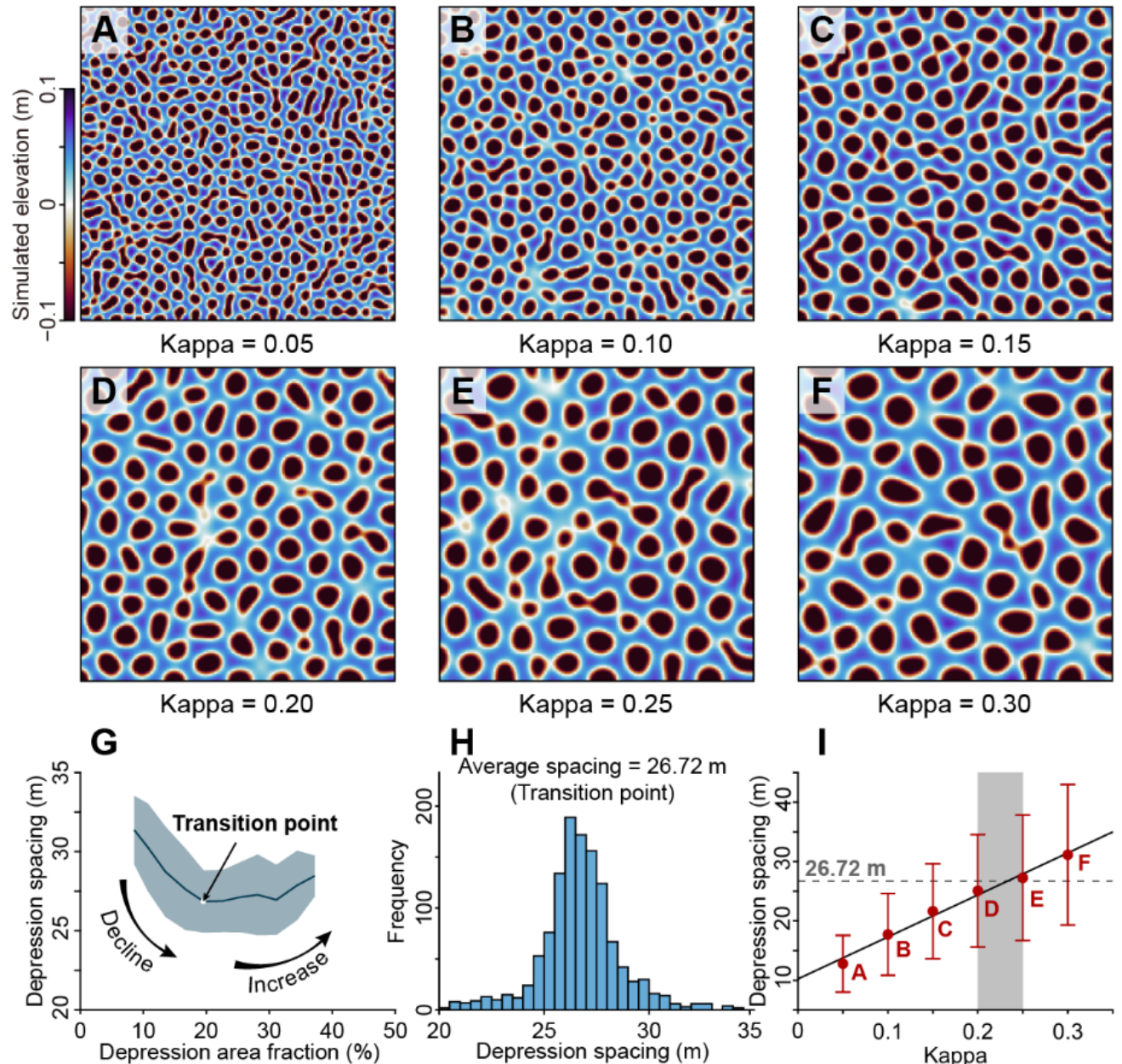


Fig. S9 Calibration of kappa parameters. **A-F**, the visualization results under different κ . The κ value used in A-F are 0.05, 0.1, 0.15, 0.20, 0.25, 0.30 respectively. The six results share a same color bar located in the left bottom of A. **G** The extraction depression spacing result of MBT in study area. The shadow region represents the SD and the blue line represent the average depression spacing. The white point represents the transition point where the average depression

spacing reaches its minimum. **H. The histogram of data points within the transition range where DAF is between 19.0% and 21.0%**. The light curve indicates the Gaussian fit curve. **I. Plot of the minimum depression spacing data acquired under varying kappa values**. The red scatters are result data points and the error bars are SD. The solid black line represents the fitted curve. ($y = 70.7606x + 10.22$, $R^2 = 0.9876$). The grey dash line represents the value average spacing acquired in H. The grey band shows the range of suitable values for kappa.

Here, the quantitative characteristics of the self-organized patterns exhibit a noticeable shift around 3.0×10^9 steps: the growth rate of DAF slows significantly, and the trend of DS changes from decreasing to increasing. Therefore, we preliminarily divide the evolution of the self-organized patterns into three stages based roughly on this 3×10^9 -step boundary: the Early Stage, the Transition Stage, and the Mature Stage. Simulations and analyses were conducted for each of these three stages respectively.

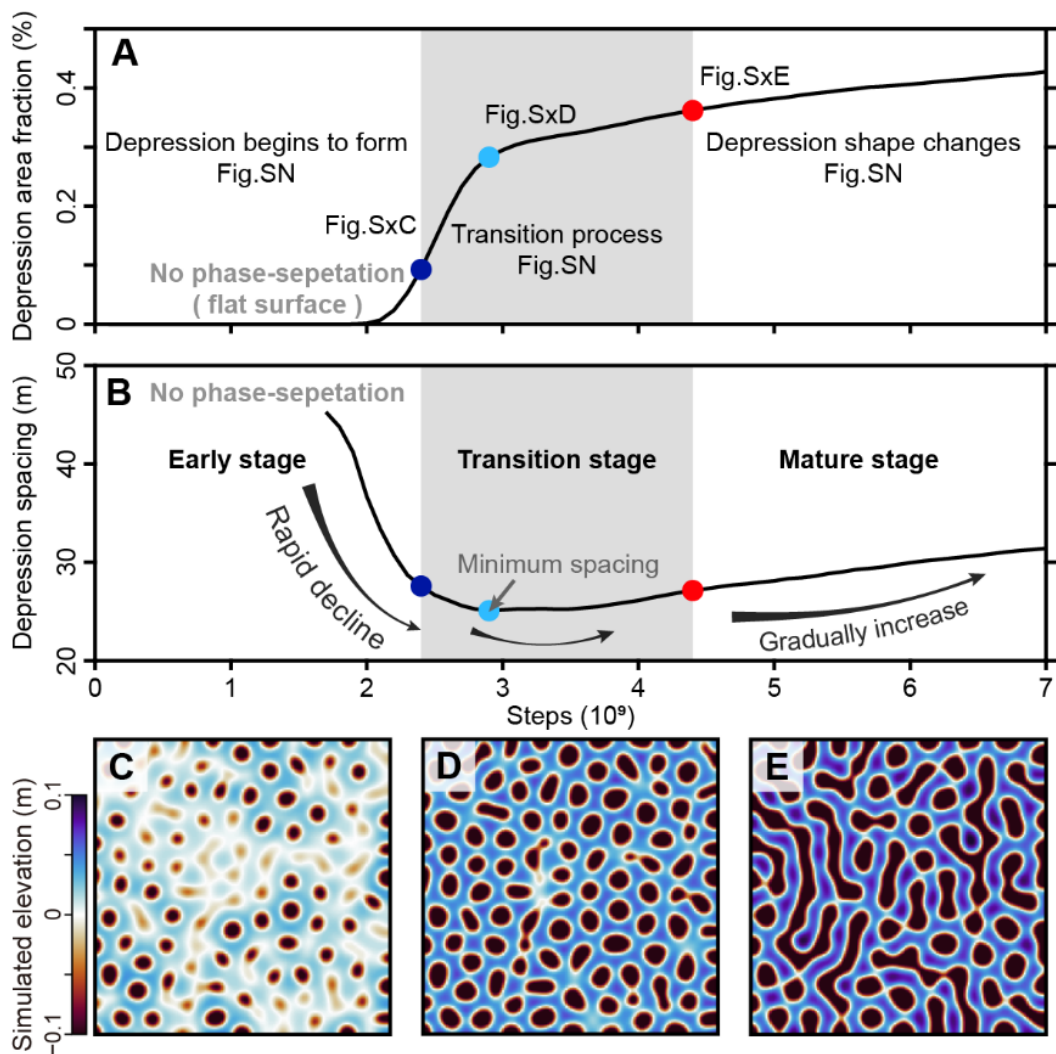


Fig. S10 The phase-separation process. A, B The plots of simulated steps vers DAF and DS respectively. The dark blue, light blue and red scatters indicate the extraction results of the self-organized patterns shown in C-E. The grey areas indicate the transition stage in both A and B. **C, D, E The self-organized patterns formed in different simulated steps ($2.8, 3.7, 4.5 \times 10^9$ steps respectively).** They share a same color bar shown in the left of C, and the region is $200 \text{ m} \times 200 \text{ m}$.

Early Stage of Self-Organized Patterns. Here, we present snapshots of several time points during the early stage of self-organization (1.0×10^9 to 2.4×10^9 steps) to observe the evolving morphological characteristics of the patterns in this phase (*SI Appendix, Fig. S11A*). We can first observe that, during the early stage, the patterns develop from non-existence to emergence. In the simulation results from 1.0×10^9 to 1.6×10^9 steps, no distinct formation is discernible, and no depressions meeting the DTE criterion are generated. This indicates that in the early stage of self-organized stone transport, due to the relatively uniform stone concentration, the stone flux driven by concentration gradients is minimal, resulting in no significant change in the concentration distribution. It can be concluded that the phase separation process has not yet initiated during this period, and the surface remains nearly flat.

When the simulation reaches 1.8×10^9 steps, we observe the localized emergence of irregular, point-like depressions whose depths meet the DTE. At this point, as these depressions are sparse and discrete, the extracted DS is predictably large. Similarly, with depressions only appearing as scattered points, the DAF is evidently low. Subsequently, between 2.2×10^9 and 2.4×10^9 steps, more irregular point-like depressions gradually appear and begin to occupy the space. Concurrently, the initially formed depressions gradually deepen and expand, transitioning from points to bubble-like shapes. During this phase, as depressions become more numerous, the DAF increases; meanwhile, their increasing spatial density leads to a gradual decrease in the DS.

Therefore, the early stage of self-organized pattern development can be summarized as: the emergence of discrete, point-like depressions, which progressively enlarge, multiply, and eventually fill the entire domain.

Transition Stage of Self-Organized Patterns. Here, we present snapshots of the self-organized patterns at different time points during the transition stage (*SI Appendix, Fig. S11B*). It can be observed that from 2.5×10^9 to 2.8×10^9 steps, the evolution of the patterns is primarily characterized by the further enlargement of bubble-like depressions and an increase in their spatial density. However, compared to the initial emergence of patterns in the early stage (1.8×10^9 to 2.4×10^9 steps), the changes during this phase are relatively subtle. This is reflected in the gradually slowing rates of increase in the DAF and decrease in the DS in the earlier part of the transition stage. During this period, pattern development remains dominated by depressions progressively occupying the available space.

Subsequently, during the 2.9 to 3.2×10^9 steps, it is notable that almost no new depressions are generated. The morphological evolution is now mainly driven by the gradual expansion and eventual coalescence of individual depressions. In this phase, the morphology of depressions transitions from discrete bubble-like shapes towards more elongated, strip-like forms. The connection and merging between adjacent depressions lead to the formation of larger, composite depressions. Throughout this process, the total depressed area continues to increase slowly, resulting in a gradual rise in the calculated DAF. Concurrently, the merging and connection of previously discrete depressions reduces the total number of distinct depression units within the domain. This reduction directly impacts the statistical calculation of DS, causing it to gradually increase.

Therefore, the development of self-organized patterns during the transition stage can be summarized as follows: the depressed area further increases; discrete bubble-like depressions become denser, enlarge, and progressively coalesce, forming larger and more complex morphological units. This evolution is quantitatively reflected in the morphological parameters as a continuous increase in DAF, accompanied by DS initially decreasing (due to denser packing of depressions) and subsequently increasing (due to their merging).

Mature Stage of Self-Organized Patterns. Here, we present snapshots of the self-organized patterns at different time points during the mature stage (*SI Appendix, Fig. S11C*). It can be observed from the figures that as the simulation steps increase, the coalescence of depressions within the patterns becomes more pronounced, leading to increasingly complex depression morphologies. This stage is characterized by merging events between depressions dominating the evolutionary process. As merging proceeds, the DAF increases slightly, while the DS rises further. Consequently, the development of self-organized patterns in the mature stage can be broadly summarized as: further coalescence among depressions accompanied by a continued, slow increase in the total depressed area.

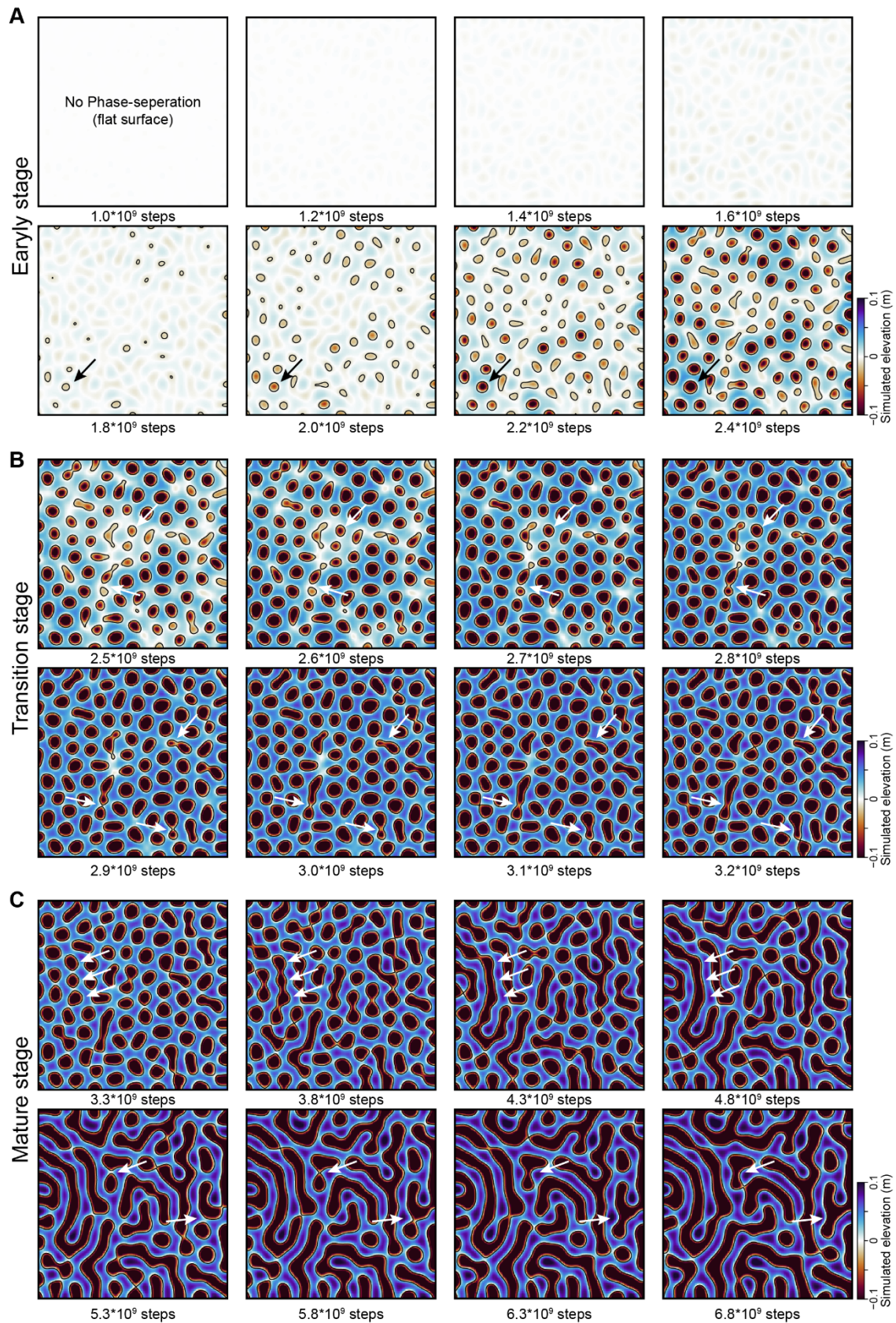


Fig. S11 the self-organized patterns formed in different stages. A, B, C represent the Early stage, Transition stage and the Mature stage respectively.

Temporal Evolution Pattern of Self-Organized Patterns. Analysis of the temporal results reveals that, within the phase-separation regime, the emergence and progressive development of depressions constitute the primary evolutionary pattern. Throughout this process, the morphological parameter DS, as defined in this study, clearly reflects a shift in the developmental objective: from “increasing the number of depressions and maximizing spatial coverage” to “deepening and merging depressions to form complex morphological units”.

A minimum value of depression spacing exists during this transition. We define the simulation step at which the depression spacing reaches this minimum as the transition point. Graphically, this point signifies that bubble-like depressions have achieved their densest possible packing within the simulation domain. Theoretically, such a transition point exists for different phase-separation modes. Therefore, we utilize this transition point as a key anchor for comparing models with different parameters (for instance, the calibration of the kappa value was performed by analyzing this specific point across different kappa parameters).

Similarity Between the Temporal Evolution of Self-Organized Patterns and MBT Morphology. Based on the analysis in the previous section, we have characterized the temporal development of self-organized patterns. Notably, the morphological changes of these patterns over time closely resemble the spatial progression of MBT observed in our study area, both exhibiting a transition from simple, bubbles-like depressions to complex morphological units. This similarity provides preliminary support for the hypothesis that self-organization may play a role in MBT formation.

However, a critical distinction must be addressed. The self-organized patterns described in the previous section are the result of temporal simulation under constant environmental parameters, representing outcomes after different durations of evolution. In contrast, the continuous morphological variation of MBT in the study area occurs within a very limited spatial extent. It is geologically implausible that MBT at different locations within such a small area would have undergone vastly different evolutionary durations. A more reasonable explanation is that: the observed spatial progression in depression morphology is caused by differential evolutionary rates of MBT resulted from spatial variations in local environmental parameters. In our constructed physical scenario, the stone transport rate is the combined result of environmental influences such as water migration, soil frost heave and needle ice growth. Therefore, in our model, the stone transport rate reflects differences in the physical environment. Thus, variations in the stone transport rate represent differences in the evolutionary rate of the MBT. Consequently, after the same total duration (i.e., the same number of freeze-thaw cycles), MBT at different locations would have reached different developmental stages (e.g., some in the transition stage, others in the mature stage).

If this scenario holds true, then by fixing the total simulation duration and analyzing self-organized patterns generated under different stone transport parameters, we should obtain a distribution of morphological characteristic parameters consistent with those measured from the actual MBT. To test this conjecture, we conducted further parameter scan analysis.

Maximum Stone Transport Rate — An Indicator of Process Activity Level. Based on the analysis in the previous section, we propose that variations in environmental parameters influence the activity level of the stone transport process, which in turn leads to morphological differences in MBT. In our constructed physical model, the activity level of the stone transport process can be characterized by the maximum stone transport rate, v_{max} . In our physical model, v_{max} represents the displacement of an isolated stone during a single freeze-thaw cycle, resulting from the combined effects of water migration, soil frost heave, and needle ice growth. As the stone is isolated, it is considered unaffected by the concentration of surrounding stones, and thus its velocity does not undergo decay. Under these conditions, the displacement depends solely on the water-ice-related processes that induce stone maximum movement. Both theoretical calculations and

laboratory experiments indicate that, given identical soil properties, increased water content enhances frost heave intensity, suggesting the potential for greater stone displacement driven by heaving (9, 10). Concurrently, a moister surface promotes stronger needle ice growth, thereby amplifying its contribution to stone transport (9, 10, 13, 14).

Regarding the study area, its limited spatial extent and overall gentle topography—lacking significant abrupt changes—allow us to assume roughly uniform physical properties of the surface sediments across the region. Based on this assumption, we further posit that the primary cause of morphological variation in MBT is the difference in the intensity of frost heave and needle ice growth, which likely reflects regional variations in water content. Consequently, we can predict that in areas with higher water content, enhanced frost heave and needle ice growth would generate greater displacement of surface stones (i.e., a larger v_{max}). A larger displacement per cycle accelerates the formation of self-organized patterns, enabling them to develop faster. Therefore, after experiencing the same number of freeze-thaw cycles, stones in areas with higher water content can form complex self-organized patterns more rapidly, whereas those in drier areas can only develop relatively simpler patterns. This concept is supported by our simulation results.

Self-Consistency of Simulation Results. *SI Appendix, Figs. S12* present a schematic of stone transport and a quantitative analysis of the simulation results. We observe that when the input parameter v_{max} is varied, the DAF of the self-organized patterns obtained after the same number of evolution steps progressively increases, indicating a rise in pattern complexity. This is consistent with our prediction proving the possibility that the complexity of MBT indicate differences in water content during its formation. Although this perspective holds considerable potential, it currently lacks sufficient constraints from additional evidence (e.g., quantitative relationships between soil water content and the transport rate of isolated stones, and quantitative relationships describing how water content influences stone transport rate by controlling needle ice growth intensity). On the one hand, this analysis demonstrates the predictive capability of the dynamic model we constructed. On the other hand, it shows that the method of simulating self-organized patterns formed under different environmental conditions by controlling v_{max} is reasonable and feasible.

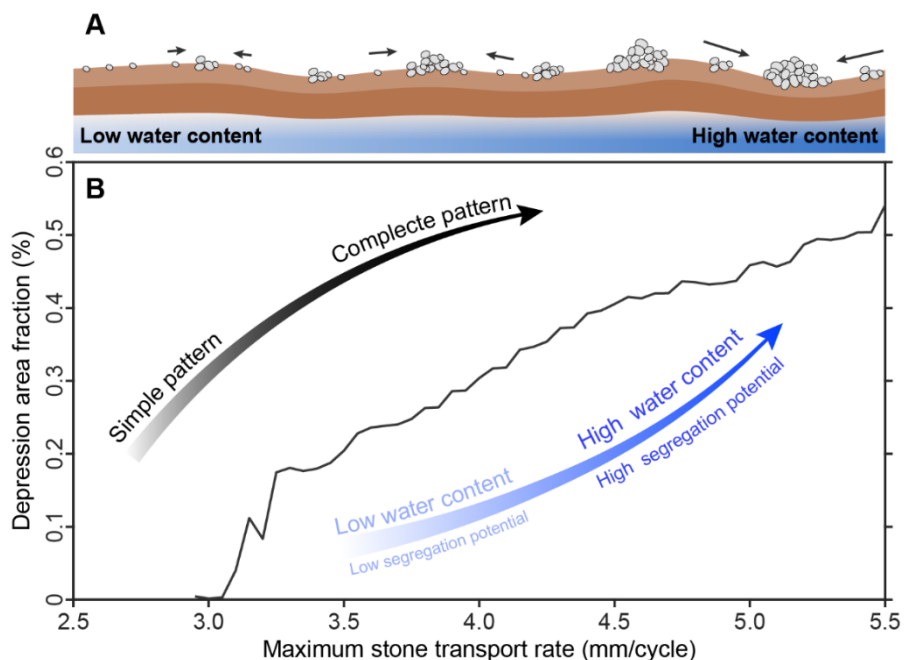


Fig. S12 Schematic Diagram of the Physical Meaning of Parameter v_{max} and Analysis Chart of Simulation Results. **A. Scene diagram of the relationship between stone transport and stone concentration.** Grey ellipses represent the

stones. The arrows indicate the direction and the displacement of stones. **B. The plot of v_{max} verse the depression area fraction.**

Fitting of Simulation Results. In the previous section, we discussed the method of simulating self-organized pattern formation under different environmental conditions by controlling v_{max} . Furthermore, we proposed that morphological differences in MBT are governed by variations in environmental parameters. Therefore, here we attempt to fit the morphology of MBT using v_{max} and the total simulation steps as the primary fitting parameters.

Parametric Scan—Simulation Steps and Maximum Stone Transport Rate. Here we show the parametric scan results of simulations run for 1×10^{10} steps under different v_{max} parameters, with the corresponding DAF, DS, and DW data extracted and visualized. From these results, it can be observed that as the input v_{max} value increases, the onset time of pattern formation occurs progressively earlier. This further validates the premise that a higher v_{max} accelerates the formation of self-organized patterns. Assuming that the MBT across the study area experienced the same evolutionary duration (i.e., a comparable number of freeze-thaw cycles), we analyze the simulation results at a fixed, identical time point.

Constraining the Time Range. Through extensive testing, we have preliminarily identified a time range of 1.7×10^9 to 3.3×10^9 steps. We separately extracted and analyzed the results at 1.7×10^9 steps, 2.5×10^9 steps, and 3.3×10^9 steps (*SI Appendix, Figs. S13A and B*). The analysis results are presented in *SI Appendix, Figs. S13D-F*. *SI Appendix, Fig. S13D* shows the DAF obtained under different v_{max} values at these three time points. *SI Appendix, Fig. S13E and F* respectively display the corresponding DAF vs. DS and DAF vs. DW relationships. From *SI Appendix, Figs. S13E and F*, it can be observed that the simulated values within the reference DAF range are comparable to the regional averages of observed MBT. Simultaneously, *SI Appendix, Fig. S13D* indicates that the v_{max} values corresponding to the reference DAF range fall within about 2.9 to 4.15 mm/cycles.

To further compare the simulation results with the measured data, we applied the same dimensional normalization procedure to the simulation results as used for the observational data. The processed results are shown in *SI Appendix, Figs. S13G and H*. The average values of DS and DW calculated during this normalization process are presented in *SI Appendix, Figs. S13I and J*.

Constraints from Dimensional Normalization Results. After applying dimensional normalization to the results from 1.0×10^9 to 4.0×10^9 steps and plotting the normalized DS and DW against DAF on scatter plots, we found that the distribution characteristics of all simulated data are consistent with those presented by the observed MBT data. Specifically, DS first decreases and then increases with rising DAF, while DW gradually increases with DAF. This trend is evident across different evolutionary times, indicating it is not a special case but rather possesses a degree of universality. The consistency between the evolutionary trend of MBT and the characteristic evolution of the self-organization process supports a self-organization genesis for MBT.

However, it is important to note that while the normalization results show consistent evolutionary trends across different step counts, this does not imply the self-organized patterns themselves are identical. A comparison of their mean values is also necessary. *SI Appendix, Figs. S13I and J* present the average DS and average DW of data points within the target range (DAF between 10% and 40%) for different step counts. From the figures, we can observe that both the statistically derived average DS and average DW continuously increase as simulation time progresses. The best match for average DS

occurs around 2.4×10^9 steps, whereas the best match for average DW appears at 1.4×10^9 steps. Here, we select the optimal match time based on DS (2.4×10^9 steps) as the target for our final simulation (the specific rationale is discussed in the next section). Consequently, we use 2.4×10^9 steps with the parameter $v_{max} = 2.90$ to 4.15 mm/cycle as the final fitting result. The corresponding result graphs are shown in the main text (Figs. 3A and B). The evolutionary trend is largely consistent with that observed in the study area's MBT.

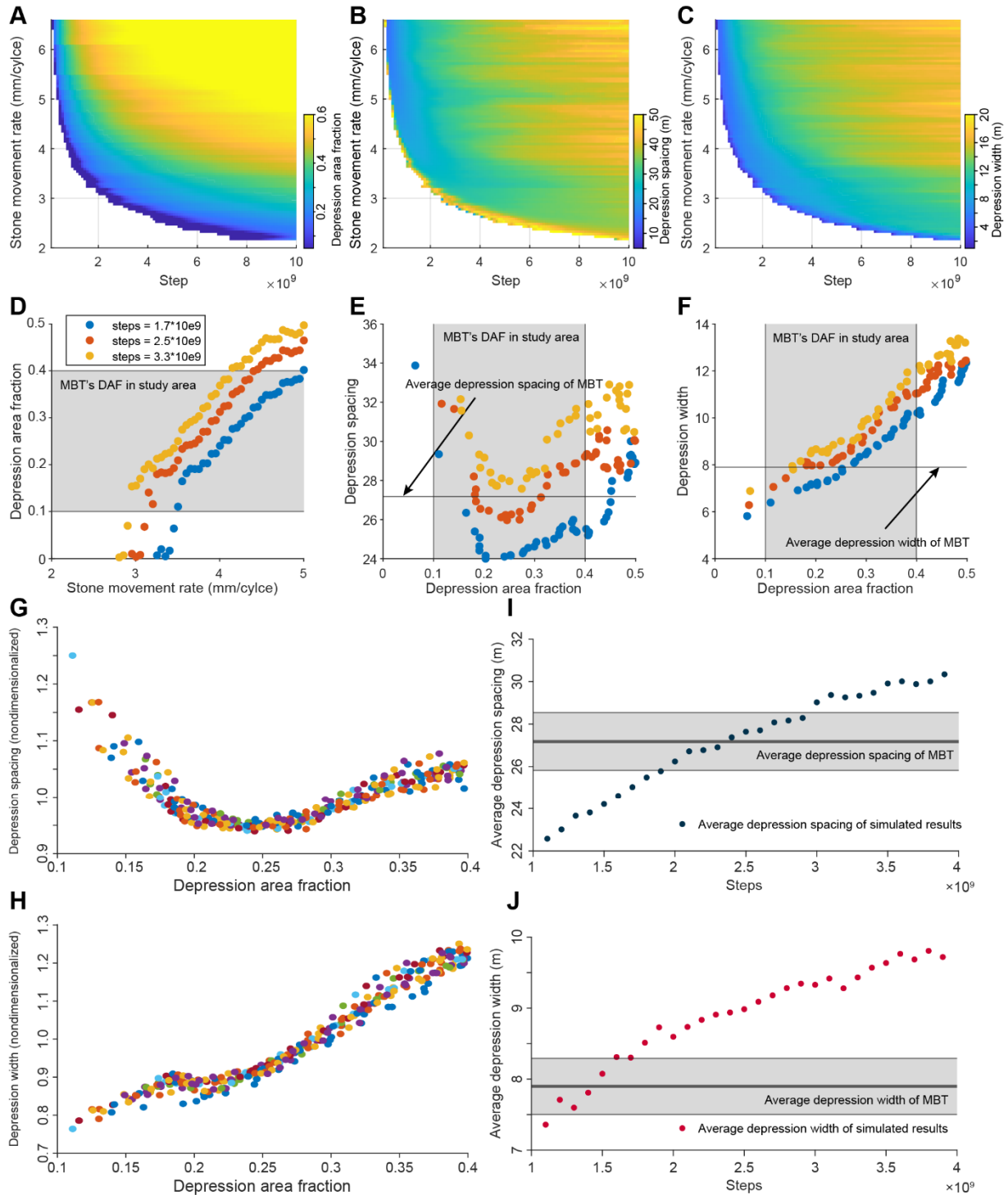


Fig. S13 Simulation result fitting flowchart. A, B, C. The parameterized scan result charts. The black lines represent the data used in D-F. D-F. The scatter plots of v_{max} verse DAF, DAF verse DS and DAF verse DW respectively. The shadow areas in D-F represent the observed MBT's DAF. The black lines in E and F represent the average DS and DW of MBT.

MBT. G. H. The scatter plots of DAF vers nondimensionalized DS and DW. I, J. The scatter plots of simulated steps versus the average DS and DW. The black lines represent the average DS and DW of MBT. The shadow areas represent the errors (SD) of average DS and DW of MBT.

Analysis of Discrepancies Between Simulation and Measured Results. Within the proposed two-stage genetic model, we posit that self-organized stone transport provides the initial framework for MBT, which is subsequently modified by sublimation processes. Therefore, the numerical simulations presented here primarily model the formation of this initial framework in the first stage. In our model, this initial framework is considered stable. During the subsequent sublimation modification, the distribution of depressions remains relatively stable; hence, the depression spacing is also relatively stable. In contrast, the sublimation process gradually deepens the depressions. This suggests that depression morphology may change during sublimation modification (e.g., collapse of the pit wall and the aeolian erosion process), which could directly alter depression width, while having a comparatively smaller impact on depression spacing. Consequently, in our proposed model, depression spacing remains relatively stable after later sublimation modification, whereas depression width has a higher likelihood of undergoing change. Therefore, when fitting the simulation results, we chose to prioritize depression spacing as the key parameter for comparison.

Vertical Analysis of the Stone Self-Organization Pattern. In the previous section, we simulated the self-organized transport process of stones using the dynamic model, capturing the temporal evolution of stone concentration within the domain. By fitting the DS, we successfully reproduced the geometric morphology of MBT. It is important to note that the output of the dynamic model is stone concentration, not elevation data, while our geometric feature extraction methodology is primarily applied to elevation data. To quantitatively compare the simulation results with the characteristic parameters of MBT, we mapped the stone concentration to elevation by constructing an idealized stone-pile model.

Idealized Stone-Pile Model. Here, we discuss an idealized conical stone-pile model (*SI Appendix*, Figs. S14). We assume that: (1) the pile is a perfect cone, (2) the cone's slope angle equals the angle of repose of the stones (θ), which is related to their properties and interlocking relationships, and (3) the cone is composed solely of stones and voids, with the volume fraction occupied by stones defined as the packing density (η). From these assumptions, we can further derive that the total mass of the cone is:

$$M_{cone} = M_{stone} = V_{cone} \cdot \varphi \cdot \rho_{stone}$$

$$V_{cone} = \frac{\pi}{3} \cdot r^2 \cdot H_{cone} = \frac{\pi}{3} \cdot H_{pile}^3 \cdot \tan\theta^{-2}$$

where V_{cone} is the volume of the stone cone, η is the packing density, θ is the angle of repose, and ρ_{stone} is the density of the stone material.

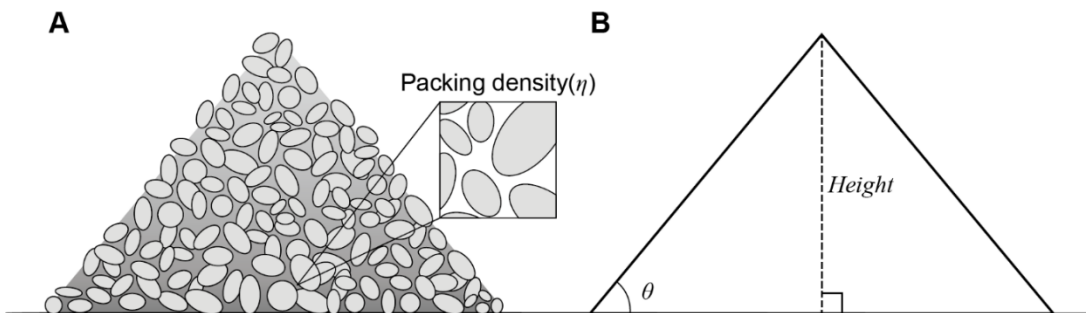


Fig. S14 Schematic diagram of an idealized stone pile model. **A.** Schematic representation of a stone pile. A local area is enlarged in the figure to illustrate the packing density (η), defined as the ratio of stone volume to the volume of the whole space. **B.** The idealized stone pile model. This model aims to approximate an irregular stone pile using a regular cone. θ denotes the angle of repose of the pile.

Stone Concentration-to-Height Mapping Relationship. Stone concentration characterizes the total mass of all stones within a given spatial area, with units of kg/m^2 . The distribution of stones in space is typically random. To discuss the maximum elevation corresponding to a given stone concentration, we consider a scenario where stones assemble to form an idealized stone pile. In this case, the stone concentration c equal to the M_{stone} and we can establish the relationship between stone concentration and the maximum height of the stone pile, yielding the following expression:

$$c = M_{\text{stone}} = \frac{\pi}{3} \cdot H_{\text{pile}}^3 \cdot \tan\theta^{-2} \cdot \eta \cdot \rho_{\text{stone}}$$

Discrepancies Between Simulation and Measured Results, and Parametric Scanning. The simulation results indicate that, under the given boundary conditions, the self-organized transport of stones can achieve a maximum stone concentration of $120.68 \text{ kg}/\text{m}^2$; and a minimum concentration of $19.39 \text{ kg}/\text{m}^2$. Assuming a pile angle of repose $= 45^\circ$ and a packing density of 60%—representing a relatively loose pile with strong interlocking—the resulting maximum elevation difference from self-organization is 0.2860 m . This is significantly lower than the measured values for MBT.

To rule out parameter influence, we analyzed the maximum pile height under different parameters (*SI Appendix*, Figs. S14). We found a positive correlation between the maximum elevation difference and the angle of repose. This suggests, in principle, that stronger interlocking and cementation between stones allow for the formation of taller piles. However, the angle of repose cannot increase indefinitely. Based on limited *in-situ* Martian observational data and studies of Martian soil simulants (15–18), the angle of repose for Martian soil is approximately 18° – 47° . For stones, where interlocking is stronger, the angle may be slightly higher, but piles in natural settings rarely exceed 50° (19, 20). Therefore, the 45° angle of repose used here likely overestimates the degree of pile cementation. Nevertheless, the calculated pile height remains below 0.5 m .

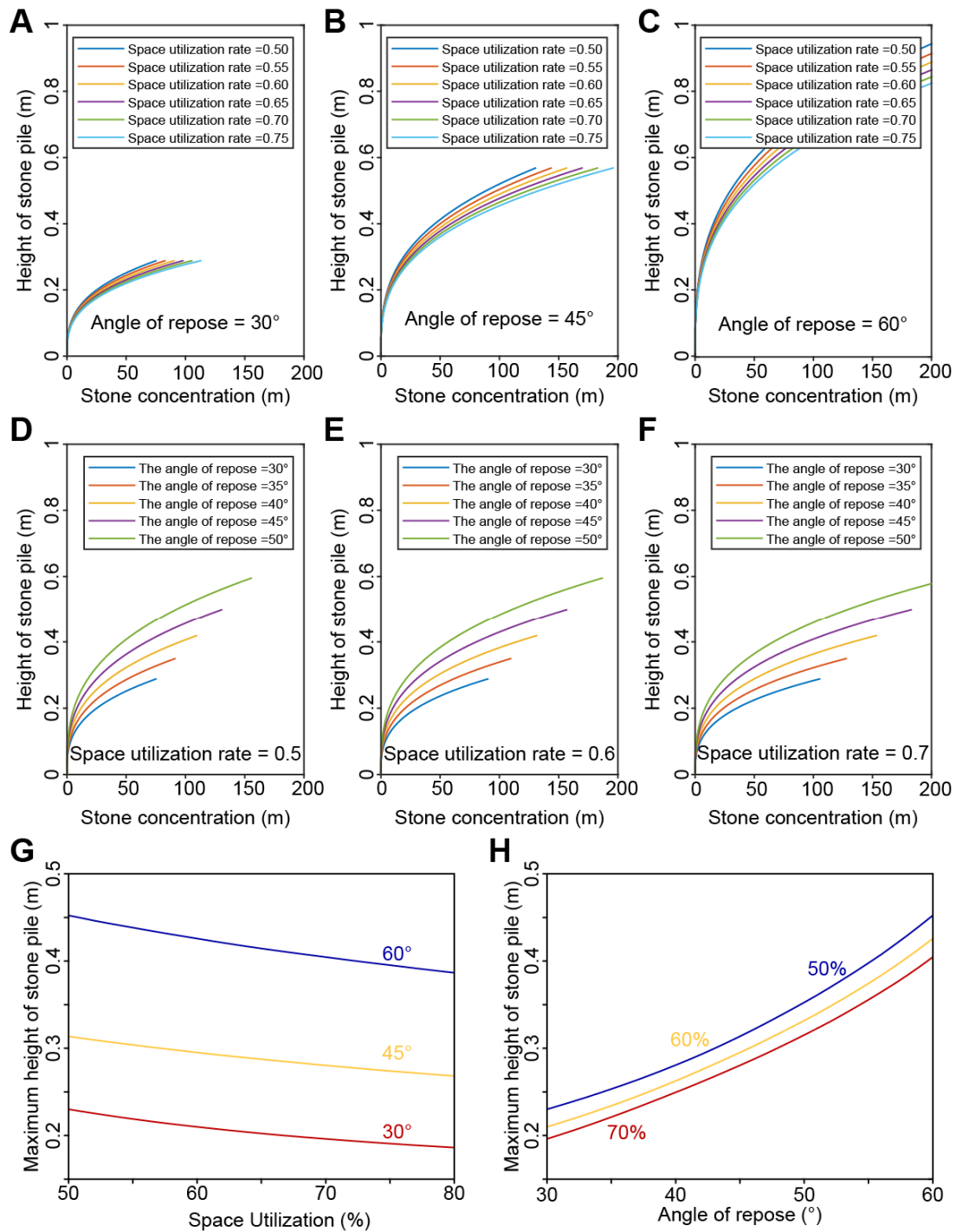


Fig. S15 The theoretical calculation of the height of stone pile.

Furthermore, we observed an inverse relationship between the maximum elevation difference and the packing density. This is because a higher packing density indicates a denser, more compact pile. For a given mass, a denser pile occupies a smaller volume, consequently resulting in a lower height. Here, we considered an extreme case with a packing density of 50%, representing an exceptionally loose pile structure, to explore the maximum possible height. Regrettably, even under this arguably unrealistic extreme condition, the maximum elevation difference of the stone pile remains below 0.5 m.

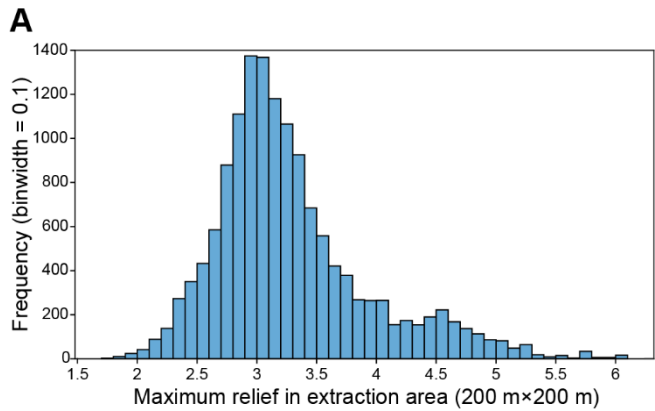


Fig. S16 Statistical Results of the Maximum Elevation Difference in the MBT Study Area

Our analysis reveals that even under the most generous assumptions, the topographic relief that can be generated by the self-organization model consistently remains less than 0.5 m. This is significantly lower than the actual observed vertical amplitude of MBT (3.29 ± 0.65 m) (*SI Appendix, Fig. S16*). Given that the self-organization model successfully reproduces the horizontal geometric morphology of MBT, we reasonably propose the existence of a subsequent modification process—likely dominated by sublimation—that amplifies the topographic relief.

Table S2. Sublimation rate on Mars

Category	Ice Type and Environmental Conditions	Typical Rate Range (mm/yr)	Method or property	Reference
Exposed Ice	Mid-latitude fresh impact-exposed ice	~1–10 ^a	Remote sensing observation	Dundas et al., 2014 (25)
Observation	Mid-latitude exposed ice cliffs	~1	Remote sensing estimate	Dundas et al., 2018 (26)
Subsurface Ice Models	Overburden (~10 cm), ice temperature 210 K	~0.1	Theoretical model calculation	Hudson et al., 2007 (27)
	Thick debris cover	<0.01	Long-term evolution model	Diniega et al., 2021 (28)
	Sublimation thermokarst formation (circular depressions)	0.008 ^a	Geomorphic evolution model	Bramson et al., 2017 (29)
Geomorphic Inversion	Total retreat of polar ice cliffs	~0.2	Observational statistical inference	Dundas et al., 2015 (30)
Rates	Phoenix landing site shallow subsurface ice (unexposed)	Net mass loss near 0	In situ detection	Fanara et al., 2020 (31)
In Situ	Phoenix landing site shallow subsurface ice (excavated and exposed)	3–7 mm per season ^b	In situ detection	Smith et al., 2009 (32)
Observations				

Table notes:

^aRate is given per Mars year.

^bEstimated range.

Reference

1. R. A. Beyer, O. Alexandrov, S. McMichael, The Ames Stereo Pipeline: NASA’s Open Source Software for Deriving and Processing Terrain Data. *Earth and Space Science* **5**, 537–548 (2018).
2. N. Mangold, Geomorphic analysis of lobate debris aprons on Mars at Mars Orbiter Camera scale: Evidence for ice sublimation initiated by fractures. *J. Geophys. Res.* **108**, 2002JE001885 (2003).
3. J. S. Levy, J. W. Head, D. R. Marchant, Concentric crater fill in Utopia Planitia: History and interaction between glacial “brain terrain” and periglacial mantle processes. *Icarus* **202**, 462–476 (2009).
4. R.-L. Cheng, H. He, J. R. Michalski, Y.-L. Li, L. Li, Brain-terrain-like features in the Qaidam Basin: Implications for various morphological features on Mars. *Icarus* **363**, 114434 (2021).
5. M. A. Kessler, B. T. Werner, Self-Organization of Sorted Patterned Ground. *Science* **299**, 380–383 (2003).
6. A. Li, *et al.*, Ice needles weave patterns of stones in freezing landscapes. *Proc. Natl. Acad. Sci. U.S.A.* **118**, e2110670118 (2021).
7. Q.-X. Liu, *et al.*, Phase separation explains a new class of self-organized spatial patterns in ecological systems. *Proc. Natl. Acad. Sci. U.S.A.* **110**, 11905–11910 (2013).
8. X. Dong, D. D. Richter, A. Thompson, J. Wang, The primacy of temporal dynamics in driving spatial self-organization of soil iron redox patterns. *Proc. Natl. Acad. Sci. U.S.A.* **120**, e2313487120 (2023).
9. N. Matsuoka, How can needle ice transport large stones? Twenty-one years of field observations. *Earth Surf. Process. Landforms* **48**, 3115–3127 (2023).
10. C. Yamagishi, N. Matsuoka, Laboratory frost sorting by needle ice: a pilot experiment on the effects of stone size and extent of surface stone cover. *Earth Surf. Process. Landforms* **40**, 502–511 (2015).
11. M. J. Schnitzer, Theory of continuum random walks and application to chemotaxis. *Phys. Rev. E* **48**, 2553 (1993).
12. P. R. Christensen, The spatial distribution of rocks on mars. *Icarus* **68**, 217–238 (1986).
13. S. Ponti, N. Cannone, M. Guglielmin, Needle ice formation, induced frost heave, and frost creep: A case study through photogrammetry at Stelvio Pass (Italian Central Alps). *CATENA* **164**, 62–70 (2018).
14. A. Li, N. Matsuoka, F. Niu, Frost sorting on slopes by needle ice: A laboratory simulation on the effect of slope gradient. *Surf. Process. Landforms* **43**, 685–694 (2018).
15. H. J. Moore, B. M. Jakosky, Viking landing sites, remote-sensing observations, and physical properties of Martian surface materials. *Icarus* **81**, 164–184 (1989).
16. G. H. Peters, *et al.*, Mojave Mars simulant—Characterization of a new geologic Mars analog. *Icarus* **197**, 470–479 (2008).

17. R. Sullivan, R. Anderson, J. Biesiadecki, T. Bond, H. Stewart, Cohesions, friction angles, and other physical properties of Martian regolith from Mars Exploration Rover wheel trenches and wheel scuffs. *J. Geophys. Res.* **116**, E02006 (2011).
18. A. Shaw, *et al.*, Phoenix soil physical properties investigation. *J. Geophys. Res.* **114**, 2009JE003455 (2009).
19. Y. C. Zhou, B. H. Xu, A. B. Yu, P. Zulli, An experimental and numerical study of the angle of repose of coarse spheres. *Powder Technology* **125**, 45–54 (2002).
20. M. A. Carrigy, EXPERIMENTS ON THE ANGLES OF REPOSE OF GRANULAR MATERIALS¹. *Sedimentology* **14**, 147–158 (1970).
21. K. A. Pearson, E. Noe, D. Zhao, A. Altinok, A. M. Morgan, Mapping “Brain Terrain” Regions on Mars Using Deep Learning. *Planet. Sci. J.* **5**, 167 (2024).
22. S. Brough, B. Hubbard, A. Hubbard, Area and volume of mid-latitude glacier-like forms on Mars. *Earth and Planetary Science Letters* **507**, 10–20 (2019).
23. J. S. Levy, C. I. Fassett, J. W. Head, C. Schwartz, J. L. Watters, Sequestered glacial ice contribution to the global Martian water budget: Geometric constraints on the volume of remnant, midlatitude debris-covered glaciers: Buried martian glaciers. *J. Geophys. Res. Planets* **119**, 2188–2196 (2014).
24. M. Golombek, D. Rapp, Size-frequency distributions of rocks on Mars and Earth analog sites: Implications for future landed missions. *J. Geophys. Res.* **102**, 4117–4129 (1997).
25. C. M. Dundas, *et al.*, HiRISE observations of new impact craters exposing Martian ground ice. *JGR Planets* **119**, 109–127 (2014).
26. C. M. Dundas, *et al.*, Exposed subsurface ice sheets in the Martian mid-latitudes. *Science* **359**, 199–201 (2018).
27. T. L. Hudson, *et al.*, Water vapor diffusion in Mars subsurface environments. *J. Geophys. Res.* **112**, 2006JE002815 (2007).
28. S. Diniega, *et al.*, Modern Mars’ geomorphological activity, driven by wind, frost, and gravity. *Geomorphology* **380**, 107627 (2021).
29. A. M. Bramson, S. Byrne, J. Bapst, Preservation of Midlatitude Ice Sheets on Mars. *JGR Planets* **122**, 2250–2266 (2017).
30. C. M. Dundas, S. Byrne, A. S. McEwen, Modeling the development of martian sublimation thermokarst landforms. *Icarus* **262**, 154–169 (2015).
31. L. Fanara, K. Gwinner, E. Hauber, J. Oberst, Present-day erosion rate of north polar scarps on Mars due to active mass wasting. *Icarus* **342**, 113434 (2020).
32. P. H. Smith, *et al.*, H₂ O at the Phoenix Landing Site. *Science* **325**, 58–61 (2009).